ISSN 8755-6839

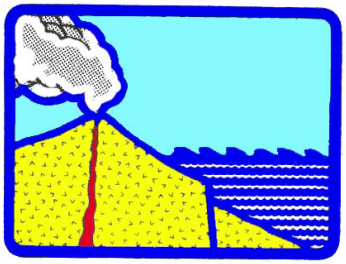

SCIENCE OF TSUNAMI HAZARDS

The International Journal of The Tsunami Society

Volume 21 Number 2 Published Electronically 2003

OBJECTIVE: **The Tsunami Society** publishes this journal to increase and disseminate knowledge about tsunamis and their hazards.

DISCLAIMER: Although these articles have been technically reviewed by peers, **The Tsunami Society** is not responsible for the veracity of any statement, opinion or consequences.

Submit manuscripts of articles, notes or letters to the Editor. If an article is accepted for publication the author(s) must submit a scan ready manuscript, a TeX or a PDF file in the journal format. Issues of the journal are published electronically in PDF format. The journal issues for 2002 are available at

http://www.sthjournal.org.

Tsunami Society members will be advised by e-mail when a new issue is available and the address for access. There are no page charges or reprints for authors.

Previous volumes of the journal are available in PDF format at

http://epubs.lanl.gov/tsunami/

and on a CD-ROM from the Society to Tsunami Society members.

ISSN 8755-6839 **http://www.sthjournal.org**

Published Electronically by The Tsunami Society in Honolulu, Hawaii, USA

.

DYNAMICS OF WATER CAVITY GENERATION

Charles L. Mader
Los Alamos National Laboratory, Los Alamos, NM 87545 USA
Michael L. Gittings
Science Applications International Corp., Los Alamos, NM 87545 USA
LA-UR-02-7735

ABSTRACT

The hypervelocity impact (1.25 to 6 km/sec) of projectiles into water has been studied at the University of Arizona by Gault and Sonett. They observed quite different behavior of the water cavity as it expanded when the atmospheric pressure was reduced from one to a tenth atmosphere. Above about a third of an atmosphere, a jet of water formed above the expanding bubble and a jet or "root" emerged below the bottom of the bubble.

Similar results were observed by Kedrinskii at the Institute of Hydrodynamics in Novosibirsk, Russia when the water cavity was generated by exploding bridge wires with jets and roots forming for normal atmospheric pressure and not for reduced pressures.

Earlier at the Los Alamos National Laboratory B. G. Craig, reported observing the formation of jets and roots while the gas cavity was expanding by bubbles generated by small spherical explosives detonated near the water surface.

During the last decade a compressible Eulerian hydrodynamic code called SAGE has been under development by the Los Alamos National Laboratory and Science Applications International (SAIC) which has continuous adaptive mesh refinement (AMR) for following shocks and contact discontinuities with a very fine grid while using a coarse grid in smooth flow regions.

A version of the SAGE code that models explosives called NOBEL has been used to model the experimental geometries of Sonett and of Craig. The experimental observations were reproduced as the atmospheric pressure was varied. When the atmospheric pressure was increased the difference between the pressure outside the ejecta plume above the water cavity and the decreasing pressure inside the water plume and cavity as it expanded resulted in the ejecta plume converging and colliding at the axis forming a jet of water proceeding above and back into the bubble cavity along the axis. The jet proceeding back thru the bubble cavity penetrates the bottom of the cavity and forms the root observed experimentally. The complicated bubble collapse and resulting cavity descent into deeper water was numerically reproduced.

Now that a code is available that can describe the experimentally observed features of projectile interaction with the ocean, we have a tool that can be used to evaluate impact landslide, projectile or asteroid interactions with the ocean and the resulting generation of tsunami waves.

.

INTRODUCTION

The process of cavity generation by projectiles or explosives in the ocean surface and the resulting fluid flows has been an important unsolved problem for over 50 years. The prediction of water waves generated by large-yield explosions and asteroid impacts has been based on extrapolation of empirical correlations of small-yield experimental data or numerical modeling assuming shallow water waves. The "upper critical depth" is an experimentally observed wave height maximum that occurs when an explosive charge is approximately two-thirds submerged. The observed height at the upper critical depth is twice that observed for completely submerged explosive charges. If the waves formed are shallow water waves capable of forming tsunamis, then the upper critical depth phenomenon would be important in evaluating the magnitude of a tsunami event from other than tectonic events. As described in reference 1 the experimentally observed waves from cavities formed by explosions near the water surface are better reproduced by models solving the incompressible Navier-Stokes equations than by modeling solving the shallow water, long wave equations. The experimentally observed waves are deep water waves. The observed upper critical depth phenomenon is apparently a result of a partition of energy near the water surface, which results in high amplitude, deep water waves (of high potential and low kinetic energy) and not the shallow water waves required for tsunamis.

During the study of the upper critical depth phenomenon in the 1960's evidence of complicated and unexpected fluid flows during water cavity formation was generated by B. G. Craig and described in references 2, 3 and 4. A sphere of explosive consisting of a 0.635 cm radius XTX 8003 (80/20 PETN/Silicon Binder) explosive and a 0.635 cm radius PBX-9404 explosive was detonated at its center. The sphere was submerged at various depth in water. PHERMEX radiographs and photographs were taken with framing and movie cameras.

While the water cavity was expanding an upward water ejecta jet was generated on the axis above the water plume and a downward water jet or root was generated on the axis below the bottom of the cavity. These results were not anticipated and neither was the observation that the water cavity proceeded to close at its top and descend down into deeper water.

It was assumed that there was something unique about the explosive source that was resulting in these remarkable observations. The reactive compressible hydrodynamic numerical models available were unable to reproduce the experimental observations or suggest any possible physical mechanisms unique to explosives.

In the early 1980's experiments were being performed at the University of Arizona to simulate asteroid impacts in the ocean. The hypervelocity impact (1.25 to 6 km/sec) of various solid spherical projectiles (Pyrex or Aluminum) into water was performed by Gault and Sonett (5). Their observations were similar to those previously observed by Craig. While the water cavity was expanding, an ejecta jet was formed at the axis above the water plume and a jet or "root" emerged along the axis below the cavity. Again the water cavity appeared to close and descend into deeper water.

So it became obvious that the earlier Craig observations were not caused by some unique feature of generation of the cavity by an explosion.

To improve the photographic resolution and reduce the light from the air shock Sonett repeated his impact experiments under reduced atmospheric pressure.

Much to everyone's surprise when the pressure was reduced from one to a tenth atmosphere, the ejecta jet and the root did not occur and the water cavity expanded and collapsed upward toward the surface. This was what had been expected to occur in both the earlier Craig experiments and the projectile impacts.

So it was evident that the atmospheric pressure and the pressure differences inside and outside the water plume above the water surface was the cause of the formation of the jet, the root and the cavity closure and descent into deeper water.

Figure 1 shows the Gault and Sonett results for a 0.25 cm diameter aluminum projectile moving at 1.8 km/sec impacting water at one atmosphere (760 mm), at 130 mm air pressure, and at 16 mm air pressure. Figure 2 shows the Gault and Sonett results for a 0.635 cm diameter aluminum projectile moving at 2.5 km/sec impacting water at one atmosphere (760 mm) and a 0.3175 cm diameter projectile moving at 2.32 km/sec impacting water at 16 mm air pressure.

Professor Kedrinskii at the Russian Institute for Hydrodynamics was also studying the generation of water cavities from exploding bridge wires (6). He was observing the formation of jets and roots as the water cavity expanded similar to those observed by Craig using explosives and by Gault and Sonett using projectiles. After we showed him the effect of reduced atmospheric pressure, he proceeded to repeat his exploding bridge wire experiments under reduced pressure. He observed that the jets and roots did not form when the atmospheric pressure was reduced to 0.2 atmosphere.

Figure 3 shows the Kedrinskii results for a exploding bridge wire in water at one atmosphere and at 0.2 atmosphere air pressure.

The different behavior of the water cavity as it expanded when the atmospheric pressure was reduced from one atmosphere to less than a third of an atmosphere is independent of the method used to generate the cavity such as a high explosive charge, an exploding bridgewire or a hypervelocity projectile impact.

These remarkable experimental observations resisted all modeling attempts for over 25 years. The numerical simulations could not describe the thin water ejecta plumes formed above the cavity or the interaction with the atmosphere on the outside of the ejecta plume and the pressure inside the expanding cavity and plume.

COMPRESSIBLE NAVIER STOKES MODELING

The projectile impact and explosive generated water cavity generation was modeled with the recently developed full Navier-Stokes AMR (Adaptive Mesh Refinement) Eulerian compressible hydrodynamic code called SAGE (7, 8, 9, 10, 11) which includes the effects of gravity. The continuous adaptive mesh refinement permits the following of shocks and contact discontinuities with a very fine grid while using a coarse grid in smooth flow regions. This allows the code to devote the bulk of the computing resources to those areas where they are needed most. It can resolve the water plume and the pressure gradients across the water plume and follow the generation of the water ejecta jet and root.

Figure 4 shows the calculated density profiles for a 0.25 cm diameter aluminum projectile moving at 2.0 km/sec impacting water at five atmosphere air pressure.

Figure 5 shows the calculated density profiles for a 0.25 cm diameter aluminum projectile moving at 2.0 km/sec impacting water at one atmosphere air pressure.

Figure 6 shows the calculated density profiles for a 0.25 cm diameter aluminum projectile moving at 2.0 km/sec impacting water at 0.1 atmosphere air pressure.

Figure 7 shows the calculated water profiles for a 0.25 cm diameter PBX-9404 explosive sphere detonated at its center half submerged in water at one atmosphere air pressure.

The computer animations are available in the file sonnet.zip at
http://t14web.lanl.gov/Staff/clm/tsunami.mve/tsunami.htm
as hyperlink "Water Cavity Generation by Projectiles and Explosives".

The experimental observations were reproduced as the atmospheric pressure was varied. When the atmospheric pressure was increased the difference between the pressure outside the ejecta plume above the water cavity and the decreasing pressure inside the water plume and cavity as it expanded resulted in the ejecta plume converging and colliding at the axis forming a jet of water proceeding above and back into the bubble cavity along the axis. The jet proceeding back thru the bubble cavity penetrates the bottom of the cavity and forms the root observed experimentally. The complicated bubble collapse and resulting descent into deeper water was also numerically modeled for the one atmosphere and higher cases.

CONCLUSIONS

In the late 1960's and early 1970's, B. G. Craig at the Los Alamos National Laboratory reported observing the formation of ejecta jets and roots by bubbles generated by small spherical explosives detonated near the water surface while the gas cavity was expanding.

The hypervelocity impact (1.25 to 6 km/sec) of projectiles into water was studied at the University of Arizona in the early 1980's by Gault and Sonett. They observed quite different behavior of the water cavity as it expanded when the atmospheric pressure was reduced from one to a tenth atmosphere. Above about a third of an atmosphere, a jet of water formed above the expanding bubble and a root developed below the bottom of the bubble. They did not occur for atmospheric pressures below a third of an atmosphere.

Similar results were observed in the middle 1980's by Kedrinskii at the Institute of Hydrodynamics in Novosibirsk, Russia when the water cavity was generated by exploding bridge wires with jets and roots forming for normal atmospheric pressure and not for reduced pressures.

During the last decade a compressible Eulerian hydrodynamic code called SAGE has been under development by the Los Alamos National Laboratory and Science Applications International (SAIC) which has continuous adaptive mesh refinement (AMR) for following shocks and contact discontinuities with a very fine grid.

A version of the SAGE code that models explosives called NOBEL has been used to model the experimental geometries of Sonett and of Craig. The experimental observations were reproduced as the atmospheric pressure was varied. When the atmospheric pressure was increased the difference between the pressure outside the ejecta plume above the water cavity and the decreasing pressure inside the water plume and cavity as it expanded resulted in the ejecta plume converging and colliding at the axis forming a jet of water proceeding above and back into the bubble cavity along the axis. The jet proceeding back thru the bubble cavity penetrated the bottom of the cavity and formed the root observed experimentally. The complicated bubble collapse was numerically modeled.

Now that a code is available that can describe the experimentally observed features of projectile interaction with the ocean, we have a tool that can be used to evaluate impact landslide, projectile or asteroid interactions with the ocean and the resulting generation of tsunami waves.

REFERENCES

1. Charles L. Mader, **Numerical Modeling of Water Waves,** University of California Press, Berkeley, California (1988).
2. Charles L. Mader, "Detonations Near The Water Surface", Los Alamos Scientific Laboratory report LA-4958 (1972).
3. Charles L. Mader, **Numerical Modeling of Detonations,** University of California Press, Berkeley, California (1979).
4. Bobby G. Craig, "Experimental Observations of Underwater Detonations Near the Water Surface", Los Alamos Scientific Laboratory report LA-5548-MS (1972).
5. Donald E. Gault and Charles P. Sonett "Laboratory Simulation of Pelagic Asteroid Impact: Atmospheric Injection, Benthic Topography, and the Surface Wave Radiation Field", Geological Society of America, Special Paper 190, pages 69-92 (1982).
6. Valery Kedrinskii, private communication (1985).
7. M. L. Gittings, "1992 SAIC's Adaptive Grid Eulerian Code", Defense Nuclear Agency Numerical Methods Symposium, 28-30 (1992).
8. R. L. Holmes, G. Dimonte, B. Fryxell, M. L. Gittings, J. W. Grove, M. Schneider, D. H. Sharp, A. L. Velikovich, R. P. Weaver and Q. Zhang, "Richtmyer-Meshkov Instability Growth: Experiment, Simulation and Theory", J. Fluid Mech. 389, 55-79 (1999).
9. R. M. Baltrusaitis, M. L. Gittings, R. P. Weaver, R. F. Benjamin and J. M. Budzinski, "Simulation of Shock-Generated Instabilities," Phys. Fluids, 8, 2471-2483 (1996).
10. Charles L. Mader, John D. Zumbro and Eric N. Ferm, "Proton Radiographic and Numerical Modelng of Colliding Diverging PBX-9502 Detonations," Twelfth International Symposium on Detonation, August 11-16, 2002, San Diego, California. Also at http://t14web.lanl.gov/Staff/clm/prad77/prad77.htm.
11. Charles L. Mader, Michael L. Gittings, "Modeling the 1958 Lituya Bay Mega Tsunami, II," Science of Tsunami Hazards, Volume 20, Number 5, pages 241-250 (2002). Also in the file litavi.zip at http://t14web.lanl.gov/Staff/clm/tsunami.mve/tsunami.htm hyperlink "Lituya Impact Landslide".

Los Alamos National Lab Contribution LA-UR-02-7735

760 mm Air

130 mm Air

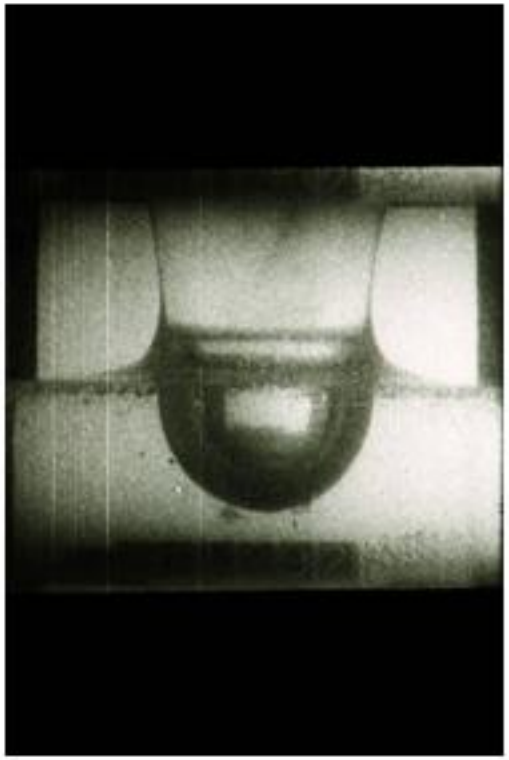

16 mm Air

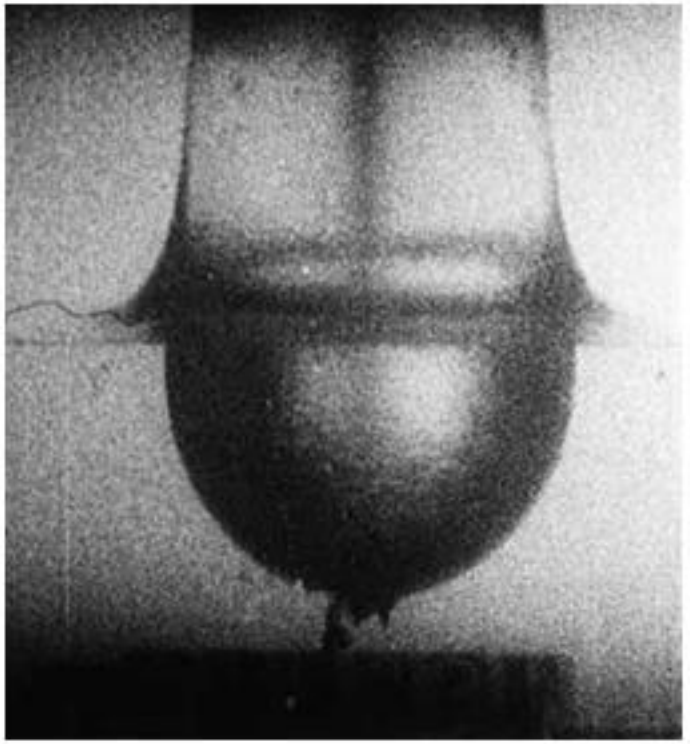

Figure 1. Gault and Sonnet results for a 0.25 cm diameter Aluminum Projectile moving at 1.8 km/sec impacting water.

760 mm Air – Al Projectile at 2.5 km/sec

16 mm Air – Pyrex Projectile at 2.32 km/sec

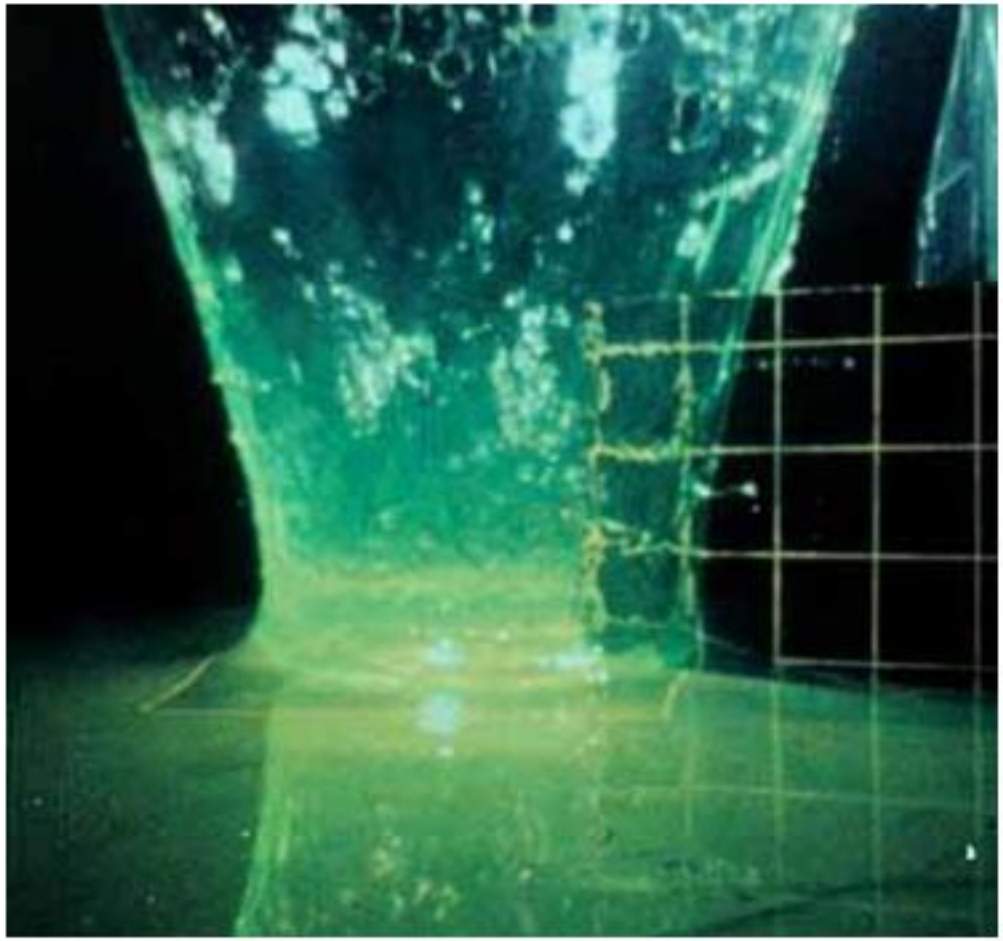

Figure 2 – Gault and Sonnet results for a 0.635 cm diameter Aluminum Projectile moving at 2.5 km/sec and for a 0.3175 diameter Pyrex Projectile moving at 2.32 km/sec

760 mm Air

150 mm Air

150 mm Air

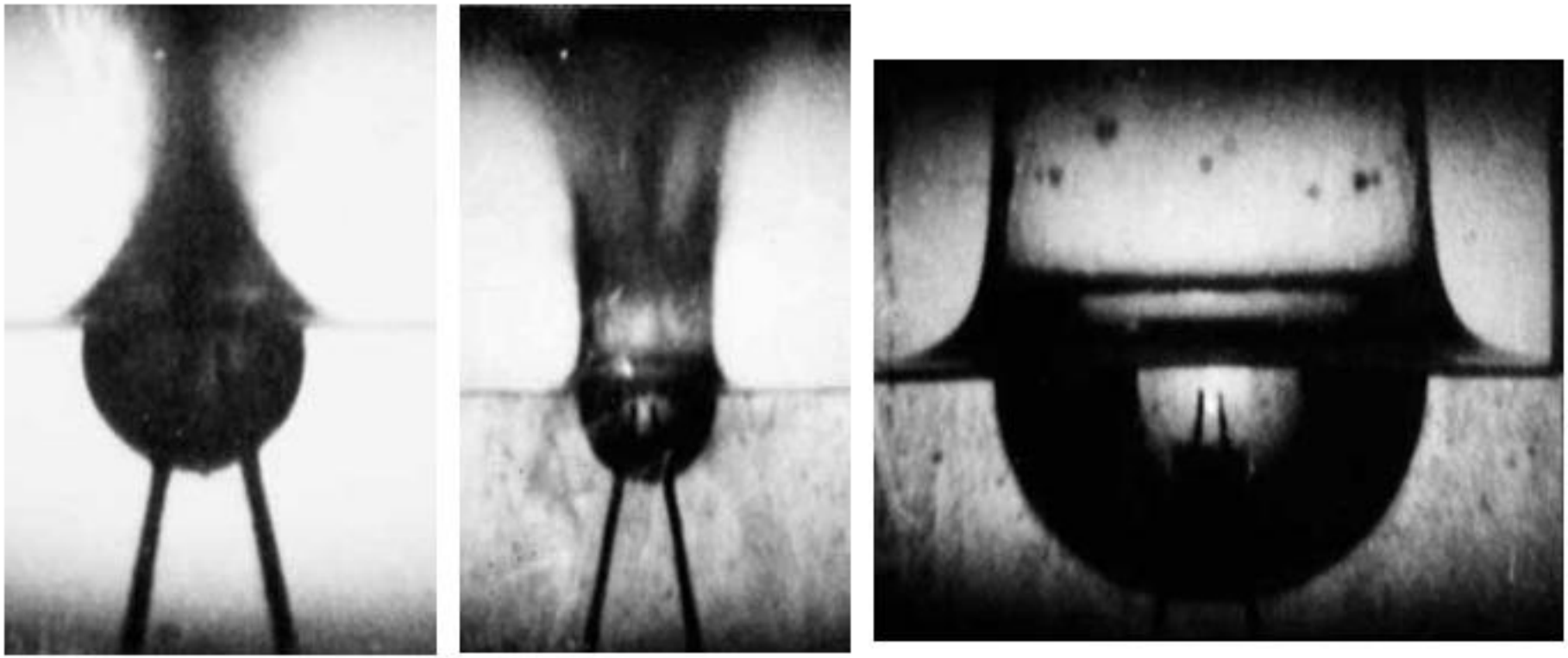

Figure 3. Kedrinskii results for an Exploding Bridge Wire in Water at 760mm and 150 mm Air Pressure.

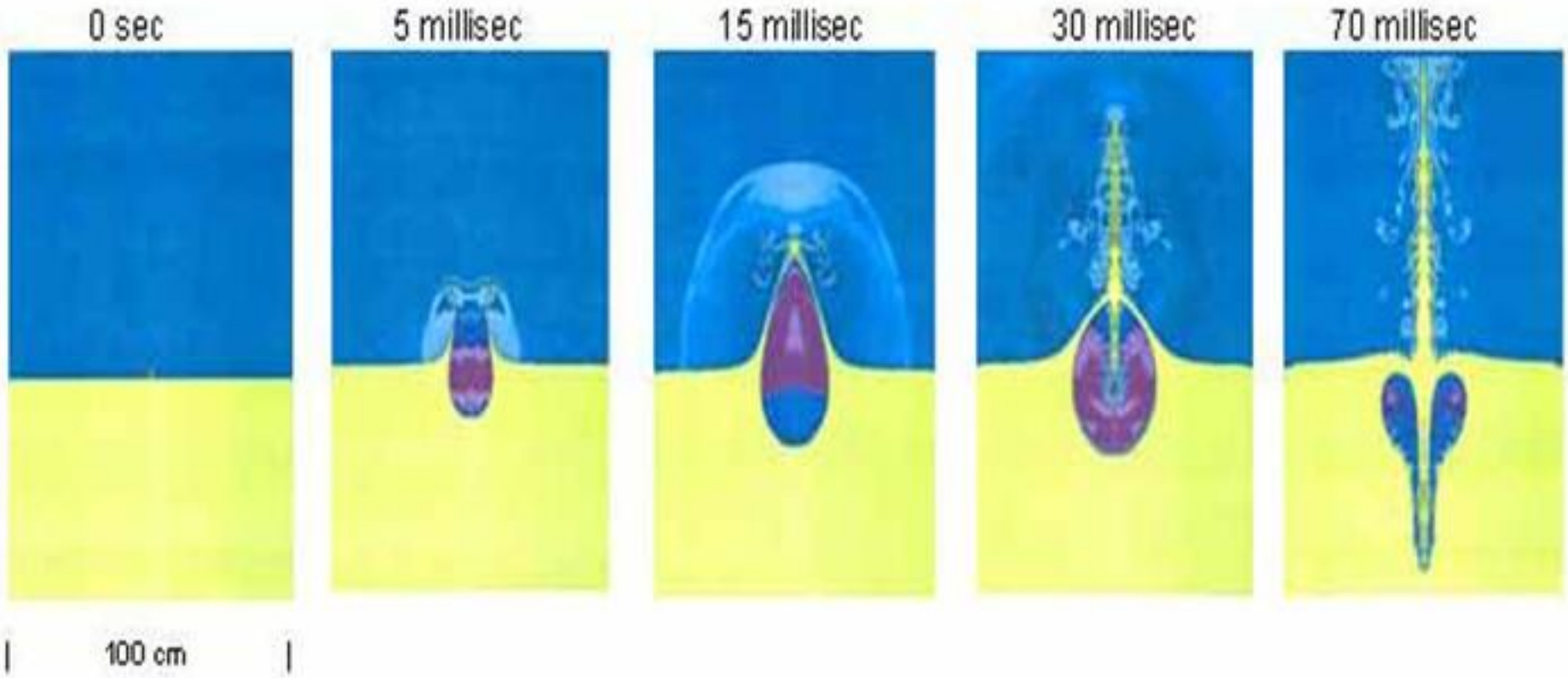

Figure 4. Density Profiles for a 0.25 cm dia Al Projectile Moving 2.0 km/sec Impacting water In Five Atmosphere Air.

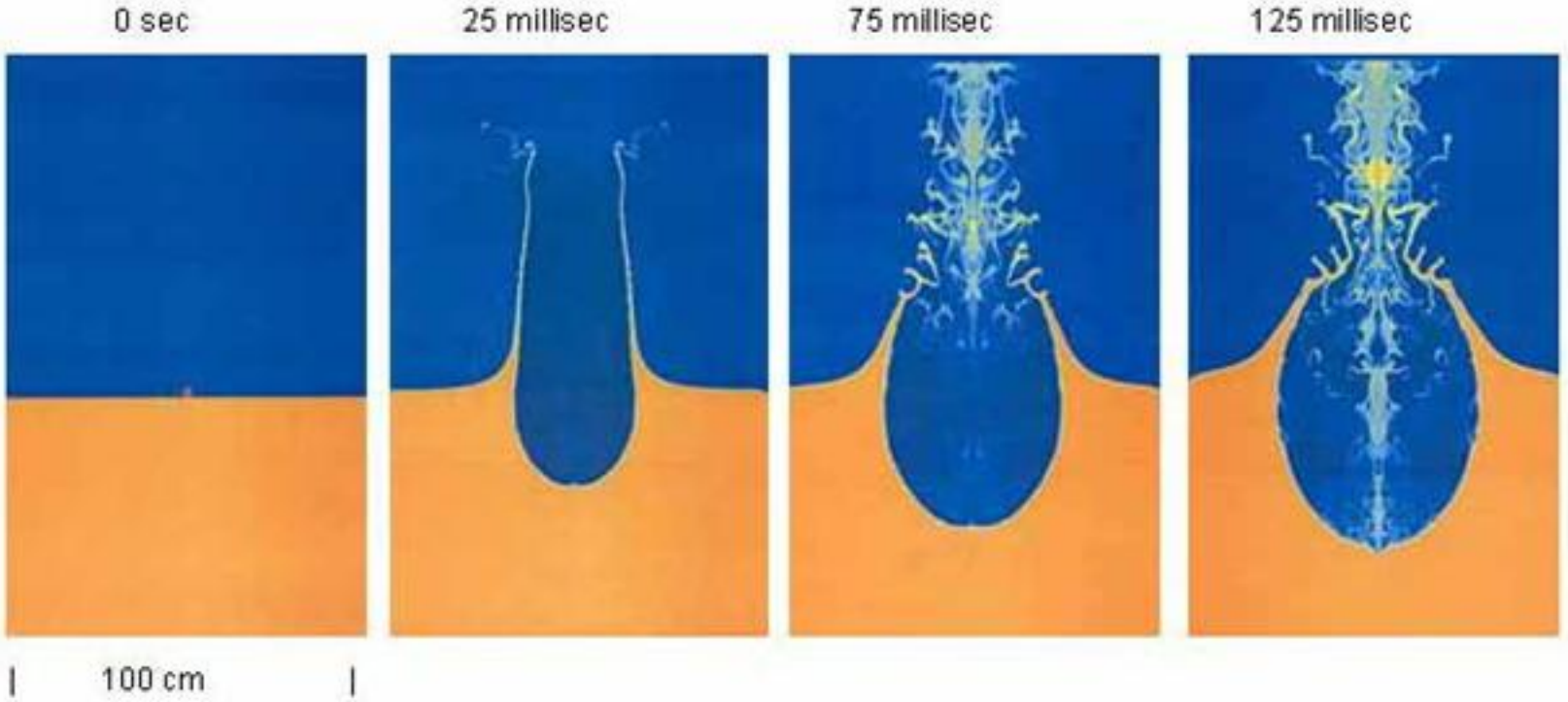

Figure 5. Density Profiles for a 0.25 cm dia Al Projectile Moving at 2.0 km/sec Impacting Water at One Atmosphere Air Pressure.

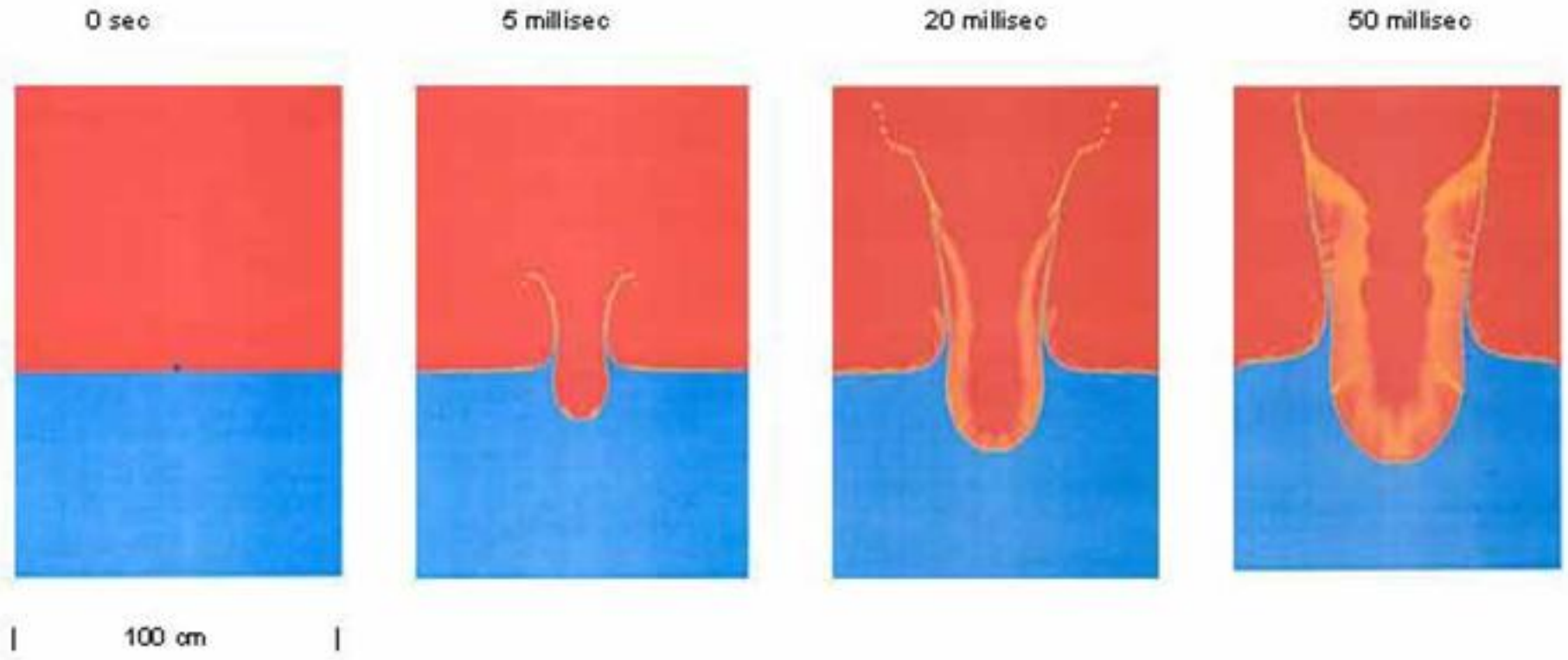

Figure 6. Density Profiles for a 0.25 cm Dia Al Projectile Moving at 2.0 km/sec Impacting Water in Air at 76 mm (0.1 atmos) Pressure.

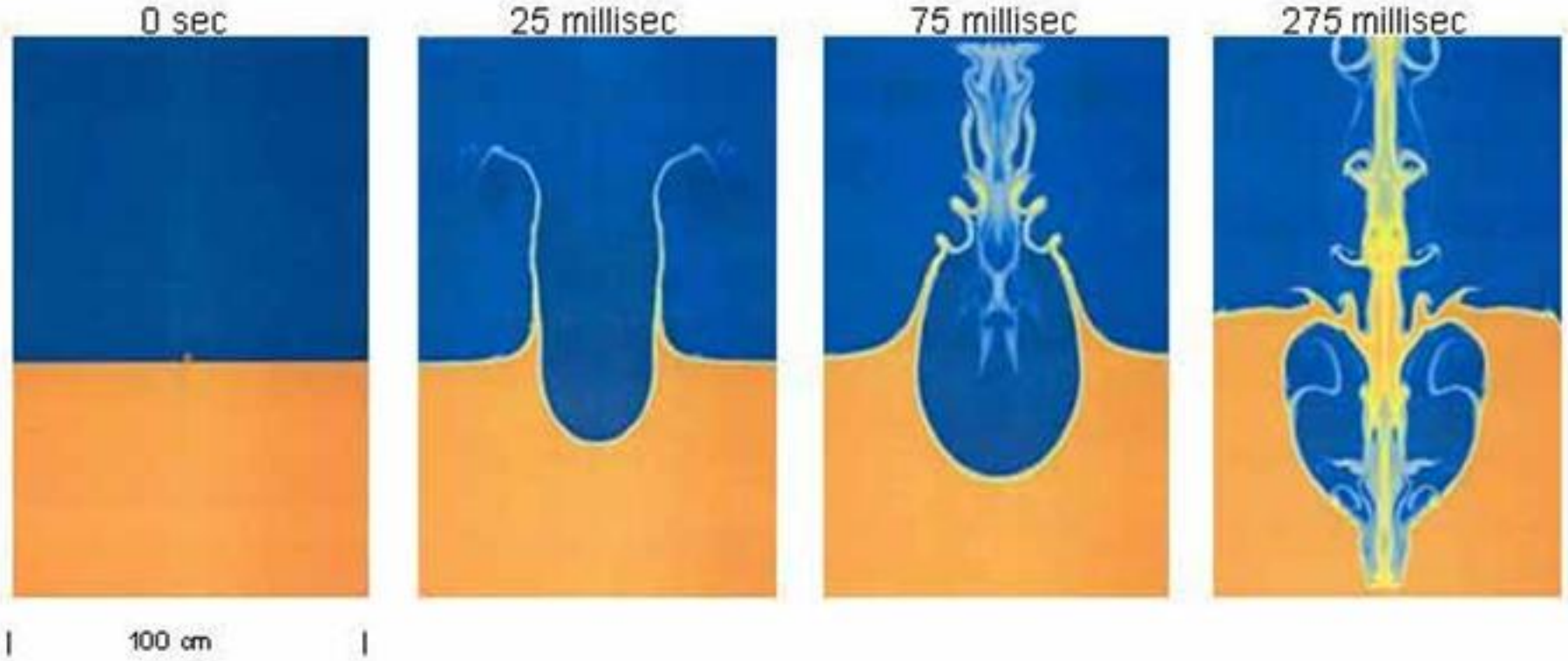

Figure 7. Density Profiles for a 0.25 cm Dia PBX-9404 Explosive Sphere Detonated at its Center and Half Submerged in Water at One Atmosphere Air Pressure.

TWO- AND THREE-DIMENSIONAL SIMULATIONS OF ASTEROID OCEAN IMPACTS

LA-UR 02-66-30

Galen Gisler, Robert Weaver, Charles Mader
Los Alamos National Laboratory
Los Alamos, NM, USA

Michael Gittings
Science Applications International
Los Alamos, NM, USA

We have performed a series of two-dimensional and three-dimensional simulations of asteroid impacts into an ocean using the SAGE code from Los Alamos National Laboratory and Science Applications International Corporation. The SAGE code is a compressible Eulerian hydrodynamics code using continuous adaptive mesh refinement for following discontinuities with a fine grid while treating the bulk of the simulation more coarsely. We have used realistic equations of state for the atmosphere, sea water, the oceanic crust, and the mantle. In two dimensions, we simulated asteroid impactors moving at 20 km/s vertically through an exponential atmosphere into a 5 km deep ocean. The impactors were composed of mantle material (3.32 g/cc) or iron (7.8 g/cc) with diameters from 250m to 10 km. In our three-dimensional runs we simulated asteroids of 1 km diameter composed of iron moving at 20 km/s at angles of 45 and 60 degrees from the vertical. All impacts, including the oblique ones, produce a large underwater cavities with nearly vertical walls followed by a collapse starting from the bottom and subsequent vertical jetting. Substantial amounts of water are vaporized and lofted high into the atmosphere. In the larger impacts, significant amounts of crustal and even mantle material are lofted as well. Tsunamis up to a kilometer in initial height are generated by the collapse of the vertical jet. These waves are initially complex in form, and interact strongly with shocks propagating through the water and the crust. The tsunami waves are followed out to 100 km from the point of impact. Their periods and wavelengths show them to be intermediate type waves, and not (in general) shallow-water waves. At great distances, the waves decay as the inverse of the distance from the impact point, ignoring sea-floor topography. For all impactors smaller than about 2 km diameter, the impacting body is highly fragmented and its remains lofted into the stratosphere with the water vapor and crustal material, hence very little trace of the impacting body should be found for most oceanic impacts. In the oblique impacts, the initial asymmetry of the transient crater and crown does not persist beyond a tsunami propagation length of 50 km.

1. Introduction

On a geological time scale, impacts of asteroids and comets with the earth must be considered as a relatively frequent occurrence, causing significant disturbances to biological communities and strongly perturbing the course of evolution. For a review of much of this work, see Pierazzo and Melosh, 2000, *Ann. Rev. Earth Planet. Sci.* 28:141. Most famous among catastrophic impacts, of course, is the one that marked the end of the Cretaceous period and the dominance of the dinosaurs.

It is now widely accepted that the worldwide sequence of mass extinctions at the Cretaceous-Tertiary (K-T) boundary 65 million years ago was directly caused by the collision of an asteroid or comet with the earth (see, e.g. Morgan et al, 2000, *Earth and Planetary Science Letters* 183:347; and Pierazzo et al., 1998, *Journal of Geophysical Research* 103:28607). Evidence for this includes the large (200 km diameter) buried impact structure at Chicxulub, Yucatan, Mexico, the world-wide distributed Iridium layer at the K-T boundary, and tsunamic deposits well inland in North America, all dated to the same epoch as the extinction event.

Consensus is building (a) that the K-T impactor was a bolide of diameter roughly 10 km, (b) that its impact was oblique (not vertical), either from the SE at 30 degrees to the horizontal or from the SW at 60 degrees, and (c) that its encounter with layers of water, anhydrite, gypsum, and calcium carbonate (all highly volatile materials at the pressures of impact) resulted in the lofting of many hundreds of cubic kilometers of these materials into the stratosphere where they resided for many years and produced a global climate deterioration that was fatal to many large-animal species on earth. All of these points are still under discussion, however, and the scientific questions that still need to be answered are (for example):

(1) How is the energy of impact (in the realm of a million gigatons TNT equivalent) partitioned among the vaporization of volatiles, the generation of tsunami, and the cratering of the substrate? How is this partition of energy reflected in the observables detectable after 65 million years?

(2) What is the fate of the projectile?

(3) How do (1) and (2) depend upon the unknown parameters of the problem, namely bolide mass, velocity, and angle of impact?

In preparation for a definitive simulation of large events like Chicxulub, we have undertaken a program of modeling smaller impacts, beginning with impacts in the deep ocean where the physics is somewhat simpler. Smaller impacts happen more frequently than the "dinosaur-killer" events, and there is evidence in the geological record for impactors of ~2 km diameter off the coast of Chile (the Eltanin event, e.g. Kyte, 2002, *Deep Sea Research II* 49:1049) and in the North Sea (Stewart & Allen, 2002, *Nature* 418:820). Besides sea-floor cratering, these events will give rise to tsunami (e.g. Ward & Asphaug, 2002, *Deep Sea Research II* 49:1073) that leave traces many kilometers inland from a coast facing the impact point.

We devote our attention in this paper to these smaller impacts, and concentrate first on

oceanic events. The same questions need to be answered as for the larger events.

This work follows on, and is influenced by, the work of Mader and Gittings (2003) on water cavity generation reported in this volume.

2. The Code

The SAGE hydrocode is an adaptive grid eulerian code with a high-resolution Godunov scheme originally developed by M.L. Gittings for Science Applications International (SAIC) and Los Alamos National Laboratory (LANL). It uses continuous adaptive mesh refinement (CAMR) by which we mean that the decision to refine the grid is made cell-by-cell and cycle-by-cycle continuously throughout the problem run. With the computing power concentrated on the regions of the problem which require high resolution, much larger computational volumes can be simulated at low cost.

It can be run in several modes of geometry and dimensionality, explicitly 1-D Cartesian and spherical, 2-D Cartesian & cylindrical, and 3-D Cartesian. A separate module for implicit, gray, non-equilibrium radiation diffusion is available but was not used in these calculations.

Because modern supercomputing is commonly done on machines or machine clusters containing many identical processors, the parallel implementation of the code is supremely important. For portability and scalability, SAGE uses the widely available Message Passing Interface (MPI). Load leveling is accomplished through the use of an adaptive cell pointer list, in which newly created daughter cells are placed immediately after the mother cells. Cells are redistributed among processors at every time step, while keeping mothers and daughters together. If there are a total of M cells and N processors, this techniques gives very nearly M / N cells per processor. As neighbor-cell variables are needed, the MPI gather / scatter routines copy those neighbor variables into local scratch.

The code incorporates multiple material equations of state (analytical or tabular) with a variety of strength models, and every cell can in principle contain a mixture of all the materials in the problem. For the asteroid ocean impact problems we used 5 materials in the problem. The first four of these are the same for all our simulations, namely air, water, basalt for the oceanic crust, and garnet for the mantle material underneath the oceanic crust. The fifth material, for the asteroid, was taken to be either dunite (3.32 g / cc) as a mockup for typical stony asteroids, or steel (7.81 g / cc) as a mockup for nickel-iron asteroids. We used tabular equations of state for the air, water, basalt, and garnet, and Mie-Grüneisen equations of state for the dunite and steel. The strength model used for the crust and asteroid are the same in all cases, namely an elasto-plastic model with shear moduli and yield stress similar to experimental values for aluminum. Only in our larger impacts is the crust penetrated, and in these we require the mantle material to have strength properties as well. For the known increase of strength with depth we use a simple pressure-hardening relationship.

3. The Simulations

Three-dimensional simulations of a 1-km diameter iron asteroid impacting the ocean at a 45-degree angle at 20 km/s were performed on the ASCI White machine at Lawrence Livermore National Laboratory, using up to 1200 processors for several weeks. Up to 200,000,000 computational cells were used, and the total computational time was 1,300,000 cpu-hours. The computational volume was a rectangular box 200 km long in the direction of the asteroid trajectory, 100 km wide, and 60 km tall. The height was divided into 42 km of atmosphere, 5 km ocean water, 7 km basalt crust, and 6 km mantle material. Using bilateral symmetry, we simulated a half-space only, the boundary of the half-space being the vertical plane containing the impact trajectory.

The asteroid is started at a point 30 km above the surface of the water (see Figure 1). The atmosphere used in this simulation is a standard exponential atmosphere, so the medium surrounding the bolide is very tenuous (density ~1.5% of sea level density) when the calculation begins. During the 2.1 seconds of the bolide's atmospheric passage at ~Mach 60, a strong shock develops, heating the air to temperatures upwards of 1 eV (1.2x10^4 K). Less than 1% of the bolide's kinetic energy (roughly 1500 Gigatons high explosive equivalent yield) is dissipated in the atmospheric passage.

The water is much more effective at slowing the asteroid, and essentially all of its kinetic energy is absorbed by the ocean and seafloor within 0.7 seconds. The water immediately surrounding the trajectory is vaporized, and the rapid expansion of the vapor cloud excavates a cavity in the water that eventually expands to a diameter of 25 km. This initial cavity is asymmetric because of the inclined trajectory of the asteroid, and the splash, or crown, is markedly higher on the side opposite the incoming trajectory (the downstream side, see Figure 2). The maximum height of the crown on the downstream side is nearly 30 km at 70 seconds after impact. The collapse of the bulk of the crown makes a "rim wave" or precursor tsunami that propagates outward, somewhat higher on the downstream side. The higher portion of the crown breaks up into droplets that fall back into the water giving this precursor tsunami a very uneven and asymmetric profile.

The rapid dissipation of the asteroid's kinetic energy is very much like an explosion, and acts to symmetrize the subsequent development. Shocks propagate outward from the cavity in the water, in the basalt crust and in the mantle beneath. Multiple reflections of shocks and acoustic waves between the material interfaces complicate the dynamics.

The hot vapor from the initial cavity expands into the atmosphere, mainly in the downstream direction because of the momentum of the asteroid (see Figure 3, which is from a run, still in progress, of a 30-degree impact). When the pressure of the vapor in the cavity has diminished sufficiently, at about 35 seconds after the impact, water begins to fill the cavity from the bottom, driven by pressure. This filling has a high degree of symmetry because of the uniform gravity responsible for the water pressure. An asymmetric fill could result from non-uniform seafloor topography, but that is not considered here. The filling water converges on the center of the cavity and the implosion produces another series of shock waves, and a jet that rises vertically in the atmosphere to a height in excess of 20 km at a time of 150 seconds after impact. It is the collapse of this central vertical jet that produces the principal tsunami wave (Figure 4).

We follow the evolution of this wave in three dimensions out to a time of 400 seconds after impact, and find that the inclined impact eventually produces a tsunami that is very nearly circularly symmetric at late times (Figure 5). The tsunami has an initial height in excess of 1 km, and declines to 100 meters at a distance of 40 km from the initial impact. Its propagation speed is 175 meters/second.

The 45-degree angle chosen for this 3-dimensional simulation is the most probable angle for impacts (Gilbert, 1893, *Bull. Philos. Cos. Wash.* 12:241). We have recently begun 3-dimensional simulations of a 30-degree impactor to better understand the dependence of the phenomenology on the angle of impact. However, because of the high degree of symmetry achieved late in the calculation, much can be learned about the physics of impact events by performing 2-dimensional simulations. Because these are much cheaper than full 3-dimensional calculations, full parameter studies can be undertaken to isolate the dependence of the phenomena on the properties of the impactor.

We have therefore performed a series of supporting calculations in two dimensions (cylindrical symmetry) for asteroids impacting the ocean vertically at 20 km/s, using the ASCI BlueMountain machines at Los Alamos National Laboratory. These simulations were designed to follow the passage of an asteroid through the atmosphere, its impact with the ocean, the cavity generation and subsequent re-collapse, and the generation of tsunami. The parameter study included 6 different asteroid masses. Stony and iron bodies of diameters 250 meters, 500 meters, and 1000 meters were used. The kinetic energies of the impacts ranged from 1 Gigatons to 200 Gigatons (high-explosive equivalent yield). An example montage from the two-dimensional parameter study is shown in Figure 6, for a 1-km iron bolide impacting vertically into a 5 km ocean. Comparison of this with Figure 1, shows that the cratering of the basalt crust is considerably enhanced for vertical impact. This is expected, since the shorter path length through the water implies less dissipation of the bolide's kinetic energy in the water before the encounter with the crust. Penetration depth may thus be an effective diagnostic of impact angle, provided other parameters can be independently determined.

A tabular summary of our parameter study is presented in Table I, in which are listed the input characteristics of the bolide (composition, diameter, density, mass, velocity and kinetic energy) and the measured characteristics of the impact (maximum depth and diameter of the transient cavity, quantity of water displaced, time of maximum cavity, maximum jet and jet rebound, tsunami wavelength and tsunami velocity.

The amount of water displaced during the formation of the cavity is found to scale very nearly linearly with the kinetic energy of the asteroid, as illustrated in Figure 8. A fraction of this displaced mass is actually vaporized during the explosive phase of the encounter, while the rest is pushed aside by the pressure of the vapor to form the crown and rim of the transient cavity.

The tsunami amplitude is also found to scale roughly linearly with the asteroid kinetic energy, and it evolves in a complex manner, eventually decaying rather faster than $1/r$ (where r is the distance of propagation from the impact point (Figure 9). The wave trains are initially highly complex (see Figure 7) because of the multiple shock

reflections and interactions involving the seafloor. Realistic seafloor topography will undoubtedly influence the development of the wave.

It is expected that the tsunami waves will eventually evolve into classic shallow-water waves (e.g. Mader, *Numerical Modeling of Water Waves*) because the wavelengths are long compared to the ocean depth. However, the complexity of the initial wave train, and the wave-breaking associated with the interaction of shocks reflected from the seafloor, do not permit the simplifications associated with shallow-water theory. Much previous work on impact-generated tsunamis (e.g. Crawford & Mader, 1998, *Science of Tsunami Hazards* 16:21) has used shallow-water theory, which gives a particularly simple form for the wave velocity, namely $v = \sqrt{(gD)}$, where g is the acceleration due to gravity and D is the water depth. For an ocean of 5 km depth, the shallow-water velocity is 221 m/s. In Figure 9 we show the wave crest positions as a function of time for the simulations in our parameter study, along with constant-velocity lines at 150 and 221 m/s. From this it is seen that the wave velocities are substantially lower than the shallow-water limit, though there is some indication of an approach to that limit at late times. This asymptotic approach is only observed for the largest impactors because the waves from the smaller impactors die off too quickly for reliable measurement in our simulations. Better measurements, with tracer particles, are in progress.

The tsunami wavelength is found to scale roughly with the 1/4 power of the asteroid kinetic energy, as shown in Figure 10. The reason for this is that the wavelength is determined by the cavity-jet-rebound cycle, and the timescale for this goes as $\sqrt{(<h>/g)}$, where $<h>$ is the mean jet height. The mean jet height, in turn, goes as the square root of the asteroid kinetic energy.

4. Recent developments and future plans

The study outlined in this paper is continuing, with a shift in focus to larger impacts and impacts in very shallow water (as at Chicxulub) and on land. For these more difficult runs it is very important to include a proper characterization of the material strength of the geological strata in which the impact occurs and the dependence of those strength properties with depth. This data is still not readily available, unfortunately. Nevertheless, we are making progress with these simulations, and hope to report on them soon.

Acknowledgments

We wish to thank Bob Greene for assistance with the visualization of the three-dimensional runs, and Anita Schwendt for help with the material strength characterization. We have also had helpful conversations with Eileen Ryan, Jay Melosh, Betty Pierazzo, Gareth Collins, and Tom Ahrens on the impact problem in general.

References

Crawford & Mader, 1998, *Science of Tsunami Hazards* 16:21.
Gilbert, 1893, *Bull. Philos. Cos. Wash.* 12:241.
Kyte, 2002, *Deep Sea Research II* 49:1049.
Mader, 1988, *Numerical Modeling of Water Waves* University of California Press.
Mader & Gittings, 2003, *Science of Tsunami Hazards 21:102.*
Morgan et al, 2000, *Earth and Planetary Science Letters* 183:347.
Pierazzo and Melosh, 2000, *Ann. Rev. Earth Planet. Sci.* 28:141.
Pierazzo et al., 1998, *Journal of Geophysical Research* 103:28607.
Stewart & Allen, 2002, *Nature* 418:820.
Ward & Asphaug, 2002, *Deep Sea Research II* 49:1073.

Table I. Summary of parameter-study runs

Asteroid material	Dunite	Iron	Dunite	Iron	Dunite	Iron
Asteroid diameter	250 m	250 m	500 m	500 m	1000 m	1000 m
Asteroid density	3.32 g/cc	7.81 g/cc	3.32 g/cc	7.81 g/cc	3.32 g/cc	7.81 g/cc
Asteroid mass	2.72e13 g	6.39e13 g	2.17e14 g	5.11e14 g	1.74 e15 g	4.09e15 g
Asteroid velocity	20 km/s	20 km/s	20 km/s	20 km/s	20 km/s	20 km/s
Kinetic energy	1.3 GT	3 GT	10 GT	24 GT	83 GT	195 GT
Maximum cavity diameter	4.4 km	5.2 km	10.0 km	12.6 km	18.6 km	25.2 km
Maximum cavity depth	2.9 km	4.3 km	4.5 km	5.7 km	6.6 km	9.7 km
Observed water displacement	4.41e16 g	9.13e16 g	3.53e17 g	7.11e17 g	1.79e18 g	4.84e18 g
Time of max cavity	13.5 s	16.0 s	22.5 s	28.0 s	28.5 s	33.0 s
Time of max jet	54.5 s	65.0 s	96.5 s	111 s	128.5 s	142 s
Time of rebound	100.5 s	118.5 s	137.5 s	162 s	187.5 s	218.5 s
Tsunami wavelength	9 km	12 km	17 km	20 km	23 km	27 km
Tsunami velocity	120 m/s	140 m/s	150 m/s	160 m/s	170 m/s	175 m/s

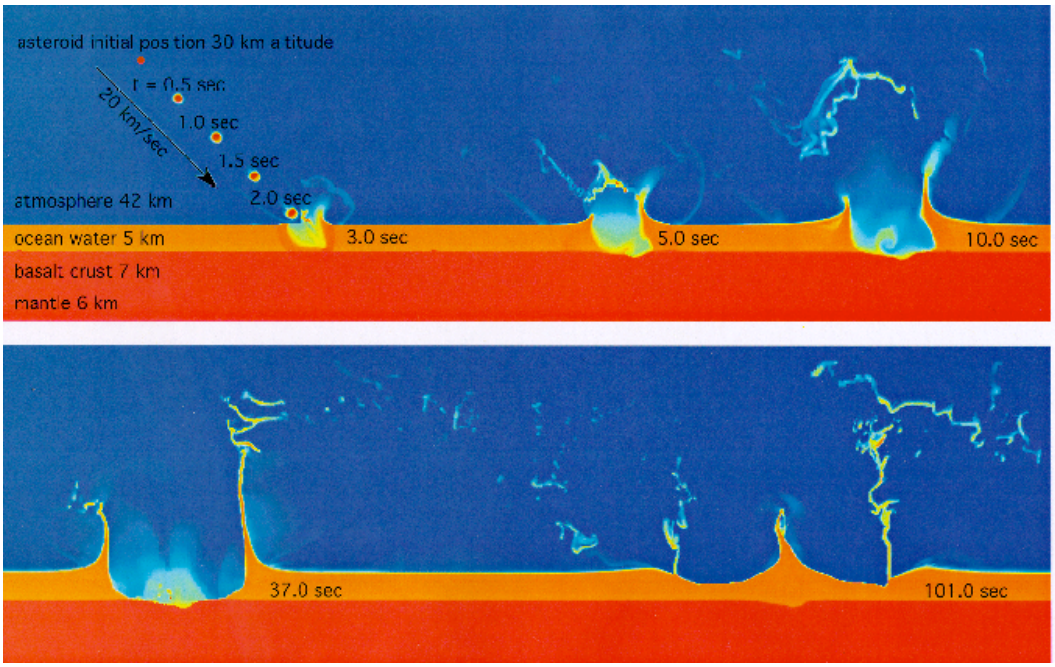

Figure 1. Montage of 9 separate images from the 3-d run of the impact of a 1-km iron bolide at an angle of 45 degrees with an ocean of 5-km depth. These are density raster graphics in a two-dimensional slice in the vertical plane containing the asteroid trajectory. Note the initial asymmetry and its disappearance in time.

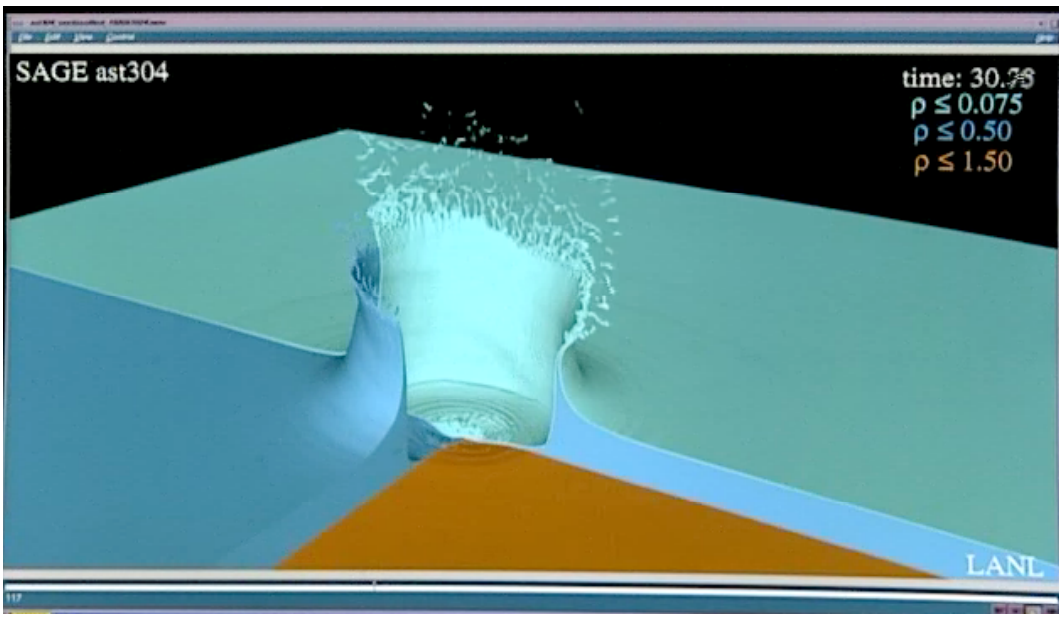

Figure 2. A perspective cutaway view from the same run illustrated in Fig. 1 at a time near the maximum cavity. The brown is the basalt crust, which is clearly cratered in this view, the blue is the water, and the green is the water-air interface. The asteroid came in from the right. Note the higher crown on the downstream side (the side opposite the impact trajectory).

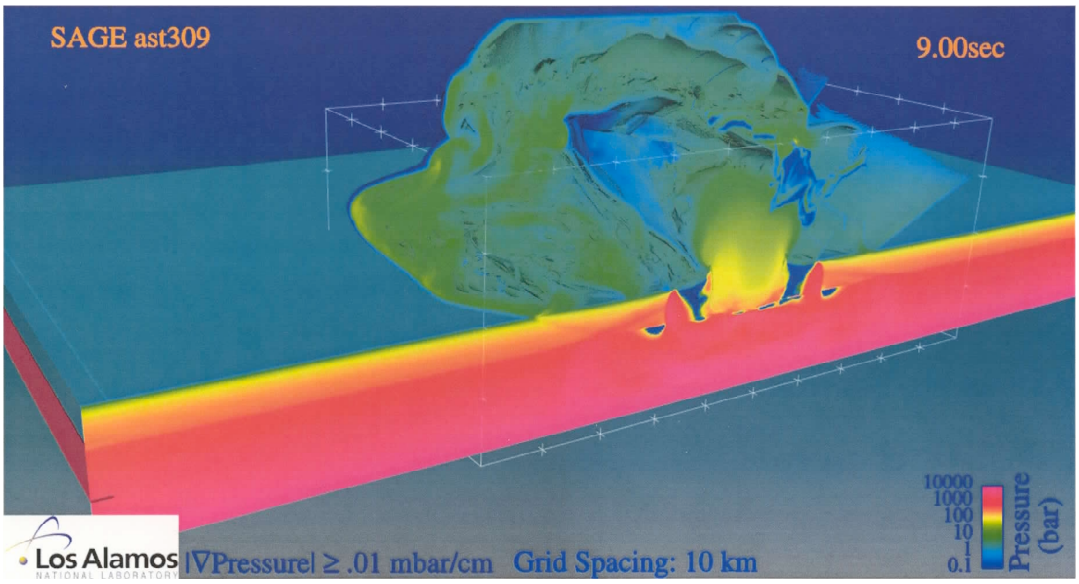

Figure 3. A pressure isosurface plot from a run of a 30 degree impactor, otherwise similar to the run depicted in Figures 1 and 2. The bolide came in from the right, and the expanding pressure wave is strongly enhanced in the downstream direction.

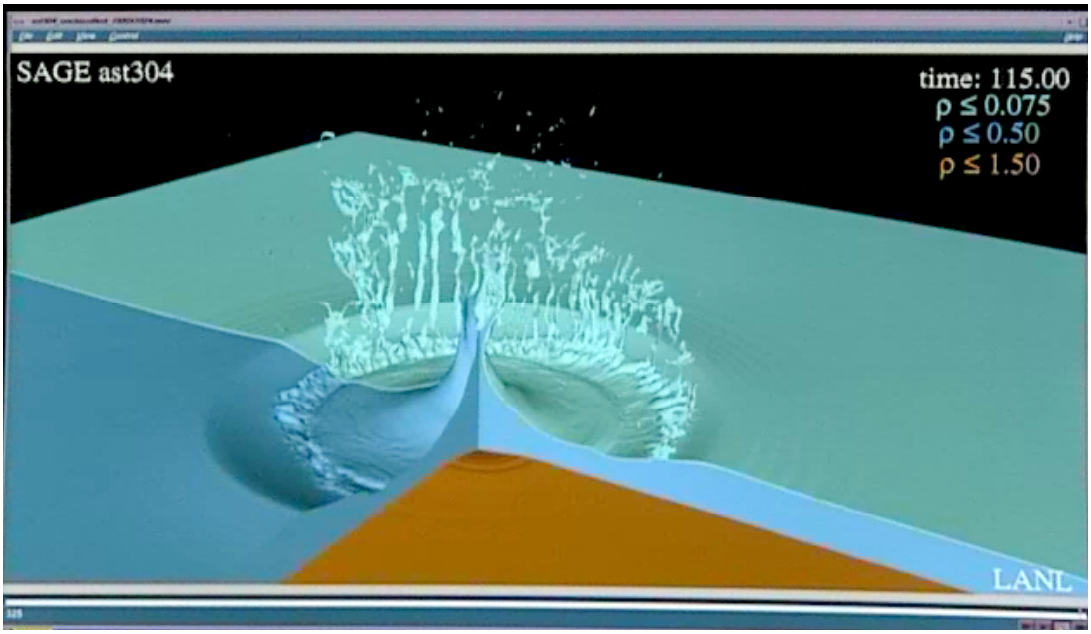

Figure 4. Similar to Fig. 2, but during the time of formation of the central vertical jet. Much of the initial asymmetry is now washed out. The collapse of the crown has produced a circular rim wave that is propagating out in all directions, but the principal tsunami wave will be produced by the collapse of the central vertical jet.

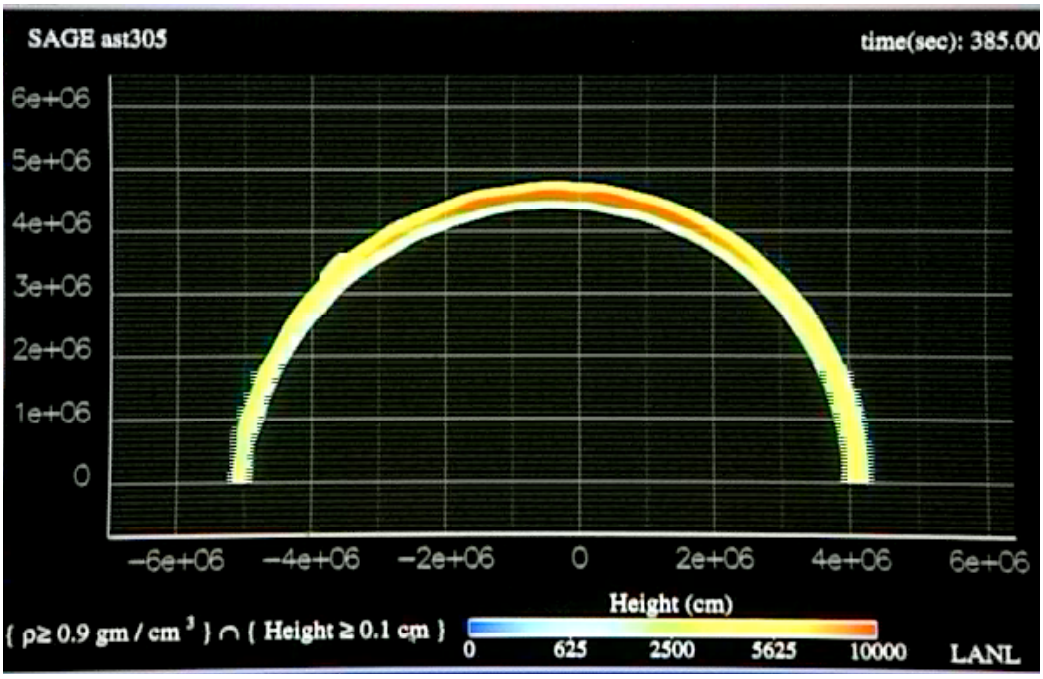

Figure 5. Overhead plot at late time showing the tsunami height as a function of x, the direction along the trajectory, and y, the direction perpendicular to the trajectory. The asteroid entered from the right. At 385 seconds, the maximum wave height is roughly 100 meters, at a distance of 40 km from the impact point.

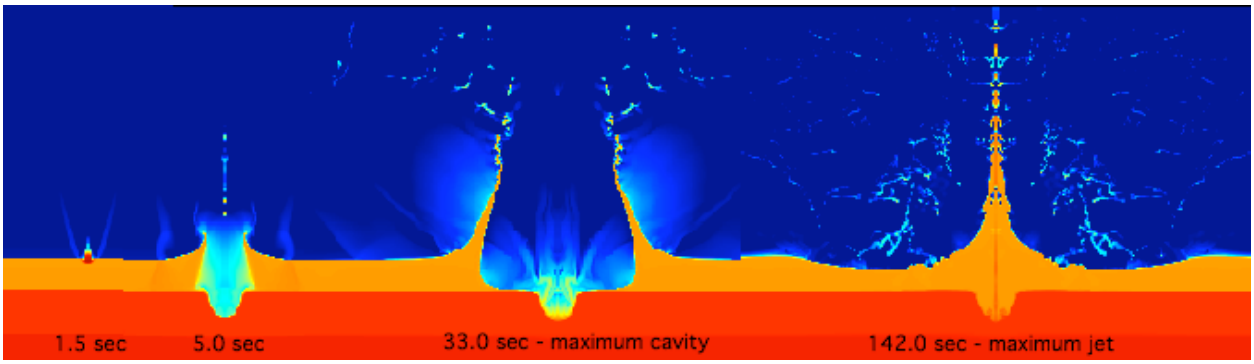

Figure 6. A 1-km iron vertical impactor craters the basalt crust, excavates a cavity in the ocean 25 km diameter, makes a vertical jet 40 km high, and a tsunami of initial amplitude 1.2 km . The excavation of the basalt is considerably greater than in the 45-degree impact, because much less of the asteroid's kinetic energy is dissipated in the water. The jetting is also considerably enhanced.

Figure 7. Portions of density plots from two different runs, shortly after the collapse of the transient crater, illustrating the complexity of the wave train. The phenomena are influenced by reflections and interactions of multiple shocks propagating through the water and the basalt crust.

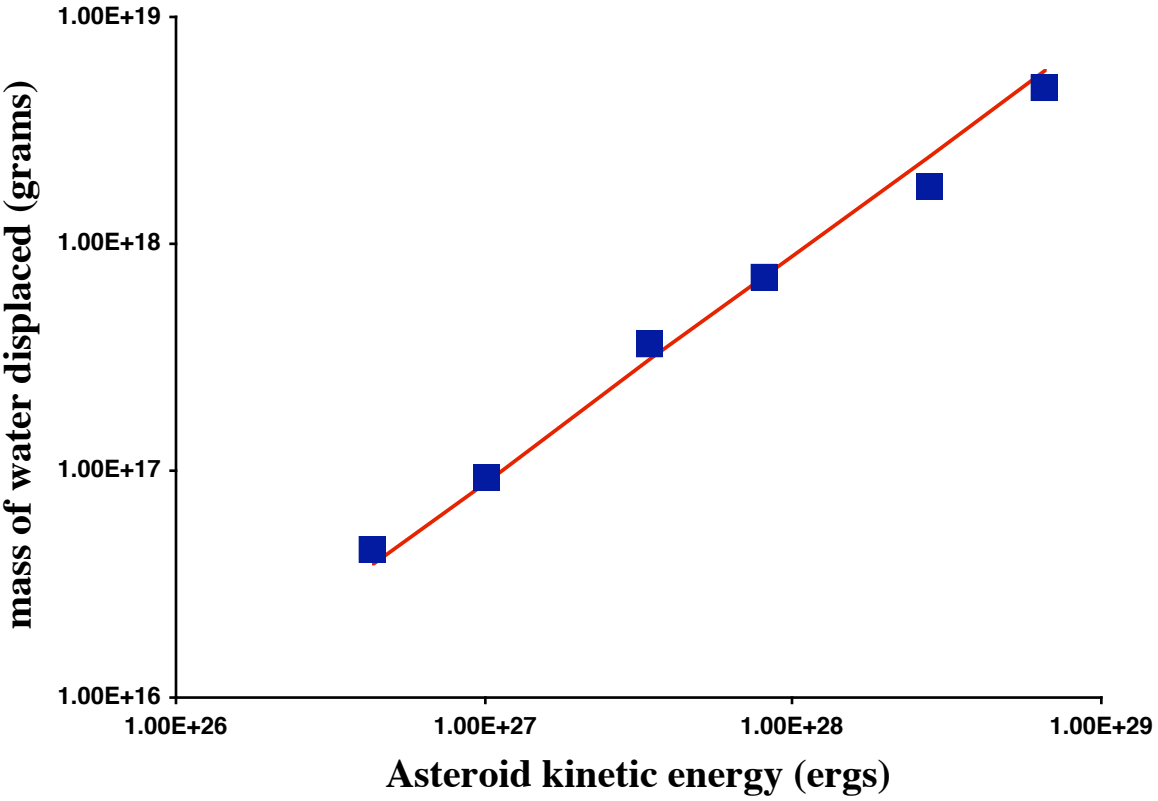

Figure 8. The mass of water displaced in the initial cavity formation scales with the asteroid kinetic energy. The squares are the results from the parameter-study simulations, as tabulated in Table I, and the solid line simply illustrates direct proportionality. A fraction (~5-20%) of this mass is vaporized in the initial encounter.

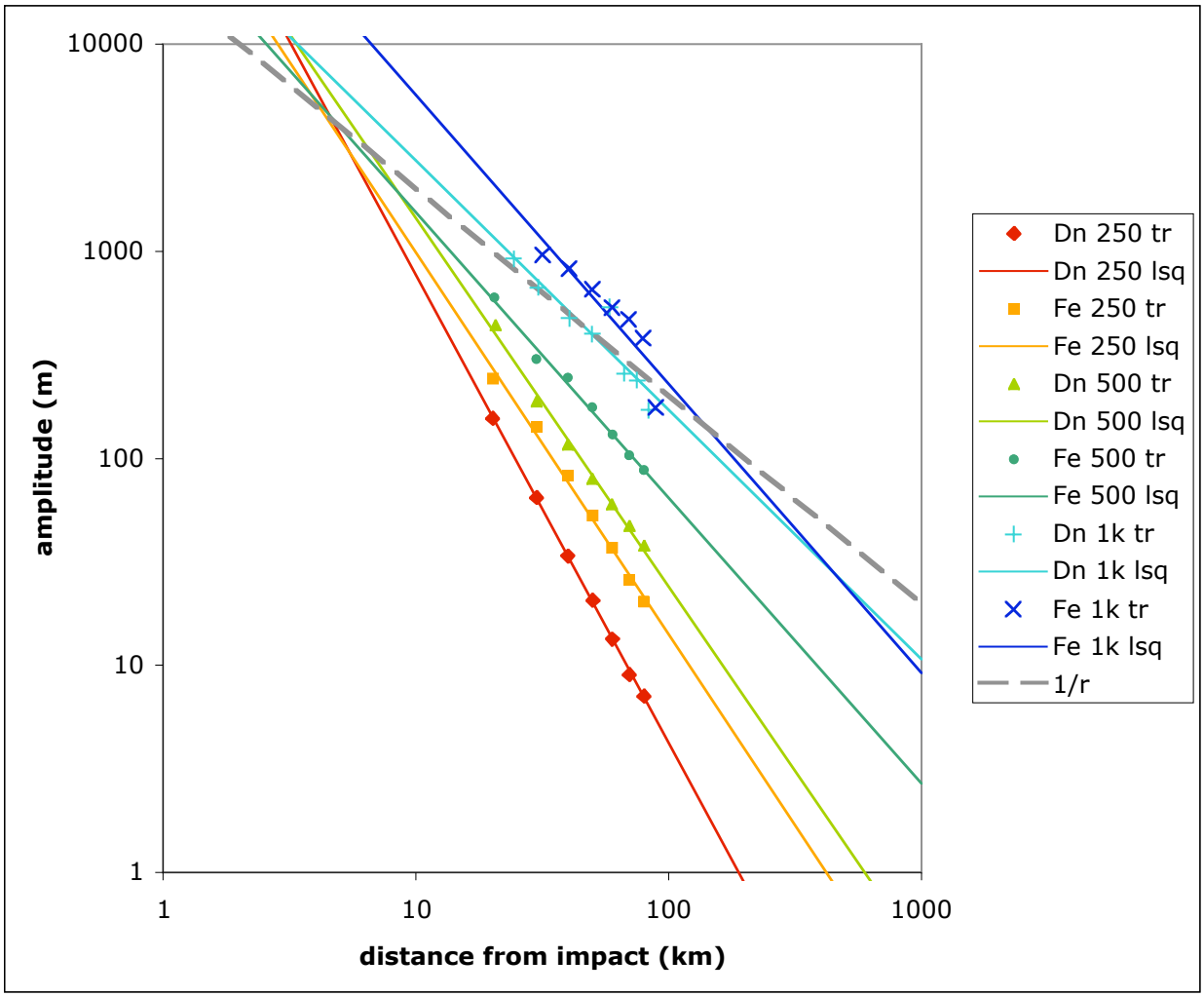

Figure 9. The tsunami amplitude scales roughly with kinetic energy and declines with distance somewhat faster than 1/r. The legend identifies the points associated with individual runs, where the notation signifies the asteroid composition ("Dn" for dunite and "Fe" for iron) and diameter in meters. For all impactors, the amplitudes were measured from tracer particles advected with the flow. Each series of points is fitted with a least-squares power-law fit whose line is also shown in the plot. The power-law indices varied from –2.25 to –1.3.

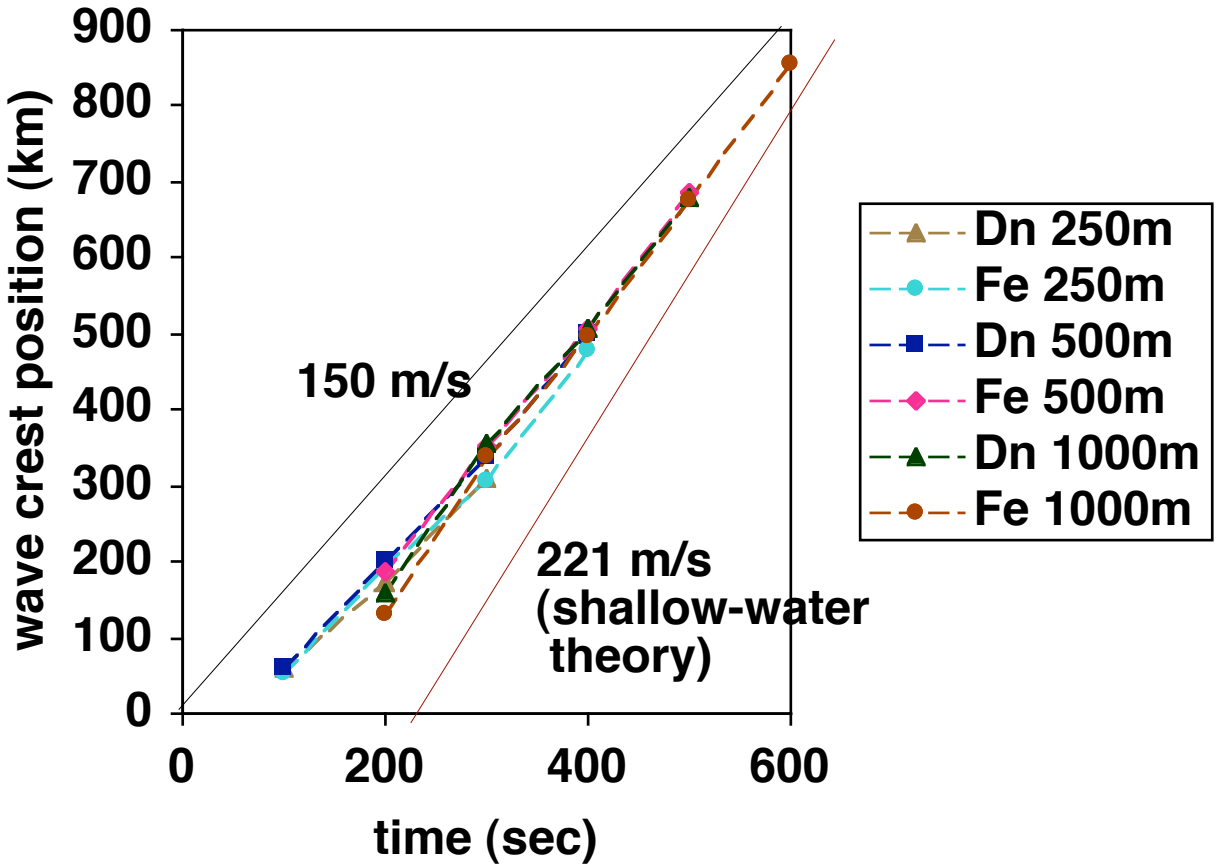

Figure 10. The tsunami wave crest positions as a function of time is here plotted for the six runs of the parameter study. The notation in the legend is the same as for Figure 8, with the solid lines at constant velocity to illustrate that these waves are substantially slower than the shallow-water theory prediction. There is an indication, however, that the waves may be accelerating towards the shallow-water limit at late times.

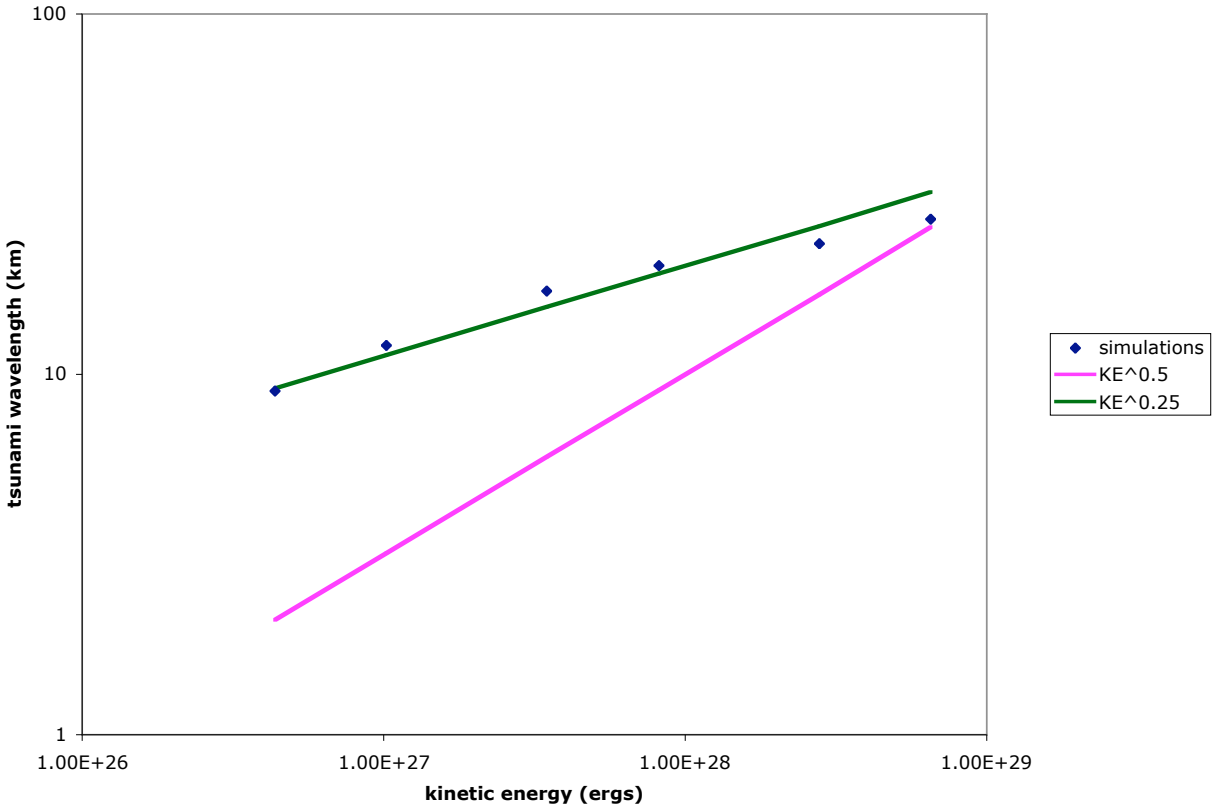

Figure 11. The tsunami wavelength as a function of the kinetic energy of the impacting asteroid. Points are from the simulations of the parameter study, as detailed in Table I, and the lines are to illustrate scalings. We find that the wavelength scales roughly with the 1/4 power of the asteroid's kinetic energy.

TSUNAMI AMPLITUDE PREDICTION DURING EVENTS: A TEST BASED ON PREVIOUS TSUNAMIS

Paul M. Whitmore
NOAA/ NWS/ West Coast/Alaska Tsunami Warning Center
910 South Felton Street
Palmer, Alaska 99645

ABSTRACT

The U.S. West Coast/Alaska Tsunami Warning Center's (WC/ATWC) far-field tsunami amplitude prediction method is tested by applying the technique to nine previous, well-recorded tsunamigenic events. Predicted tsunami amplitudes outside the source area are shown to be sufficiently accurate to guide warning cancellation/restriction/expansion decisions. Average error per event ranged from 0.04m to 0.29m with error defined as the absolute value of the difference between the recorded amplitude and the predicted amplitude. Had this technique been available during the 1986 Aleutian Is. and the 1994 Kuril Is. tsunami warnings, the warned areas likely would not have been expanded to include the U.S. West Coast, Canada, and Alaska east of Kodiak Island.

Science of Tsunami Hazards, Volume 21, page 135 (2003)

PREDICTION METHOD SUMMARY

The basic tsunami modeling technique used in the WC/ATWC far-field prediction method is described by Kowalik and Whitmore (1991). Initial tsunami profile is computed from fault dislocation formulae of Okada (1985). Waves are propagated using the shallow-water wave equations with non-linear terms and friction included in areas of fine grid resolution. An explicit-in-time finite difference scheme is used with grid increments of 5' over the deep ocean, 1' over the shelf and 12" where necessary to describe near-shore coastline configuration. All grids interact dynamically throughout the computations. The ocean/land boundary is fixed. That is, inundation is not taken into account.

The methodology which utilizes models computed as described above to predict far-field tsunami amplitudes is described by Whitmore and Sokolowski (1996). To summarize, tsunami models are computed for 204 hypothetical earthquakes along the coasts of northern Honshu, Kuril Is., Kamchatka, Aleutian Is., Alaska, British Columbia, Cascadia, and Chile. The hypothetical earthquake source parameters are determined by regional tectonic setting and past earthquakes. Moment magnitudes range from 7.5 to 9.5. Figure 1 shows modeled fault locations.

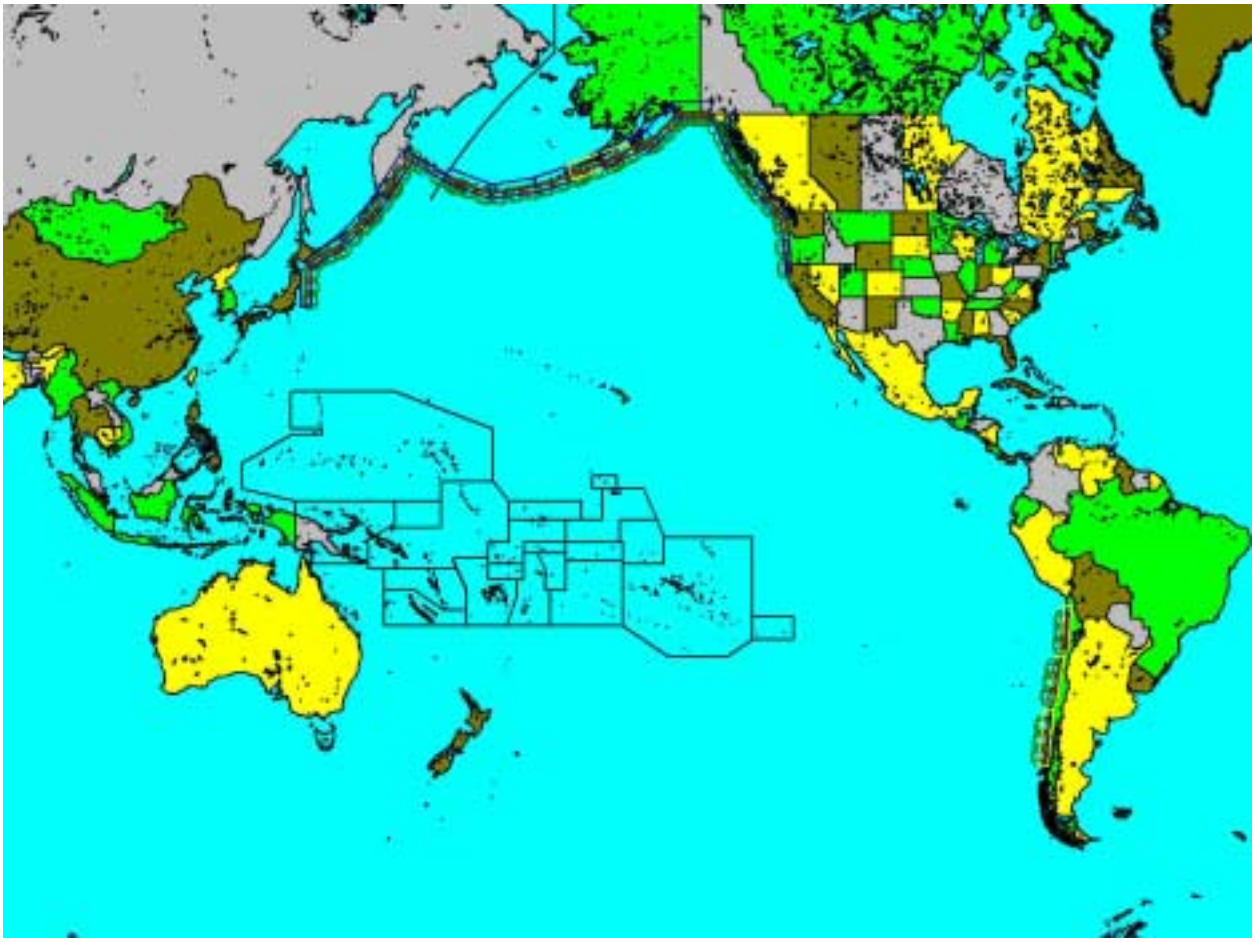

Figure 1. Model fault zones: yellow boxes represent Mw=9.5 models, blue boxes represent Mw=9.0 models, red boxes represent Mw=8.2 models, and green circles represent Mw=7.5 models.

Maximum modeled amplitudes (amplitude defined as zero-to-peak distance in meters) are saved at 99 locations along the Pacific coasts of Alaska, British Columbia, Washington, Oregon, California, Hawaii, and at the DART buoys (Bernard, *et al.*, 2001) for each of the 204 models. During a tsunami warning, the model closest to the epicenter with the nearest moment magnitude is chosen. The previously computed amplitudes at all modeled sites are scaled as the tsunami is recorded on tide gages or DART recorders by simple proportions. Scaling can only be performed with data from gages which were included in the models. As the tsunami progresses, scaling factors are averaged. The predicted tsunami amplitudes are the scaled modeled results. Model results are not trusted until scaled with an observed tsunami.

TEST RESULTS

The predictive methodology is tested on nine historic tsunamis. Events tested are those that had moderate-sized or greater tsunamis in the WC/ATWC area-of-responsibility (AOR – Alaska, British Columbia, Washington, Oregon, and California), and were well-recorded on tide gages. Only tsunami amplitudes from tide gages are used for comparison and scaling as the modeling technique does not account for inundation (i.e., runup heights are not used for comparison). A wide variety of tsunami events are tested. Moderate size tsunamis, large tsunamis, and a tsunami produced by a "tsunami" earthquake are tested. In each case the model closest to the epicenter in distance and closest to the earthquake in moment magnitude is chosen. Amplitude data from the nearest 2 to 4 tide gages are used to scale the chosen model. The number of scaling stations depends on tide gage availability around the source. Table 1 is a summary of the average error, maximum error, number of scaling sites, and the scaling factor for each tested event. Error is defined as the absolute value of the difference between the recorded and modeled amplitudes. Figure 2 shows a summary of individual tide gage/model comparisons along with scaling sites for each event.

Source Region	Date	# Scaling Sites	Scale Factor	# Observations	Maximum Error (m)	Average Error (m)
Peru	2001/6/23	2	0.86	19	0.12	0.04
Kuril Is.	1994/10/4	3	0.94	20	0.26	0.06
Aleutian Is.	1986/5/7	4	0.59	7	0.47	0.11
Rat Is.	1965/2/4	4	0.25	6	0.18	0.09
Gulf of Alaska	1964/3/28	3	1.69	21	0.76	0.28
Southern Chile	1960/5/22	4	1.07	17	1.52	0.29
Aleutian Is.	1957/3/9	3	1.84	16	0.40	0.13
Kamchatka	1952/11/4	3	1.14	17	1.20	0.25
Alaska Peninsula	1946/4/1	3	3.42	10	0.72	0.26

Table 1. Predicted amplitude error summary for each of the nine tested tsunamigenic events. Comparisons for individual observations are shown in Figure 2.

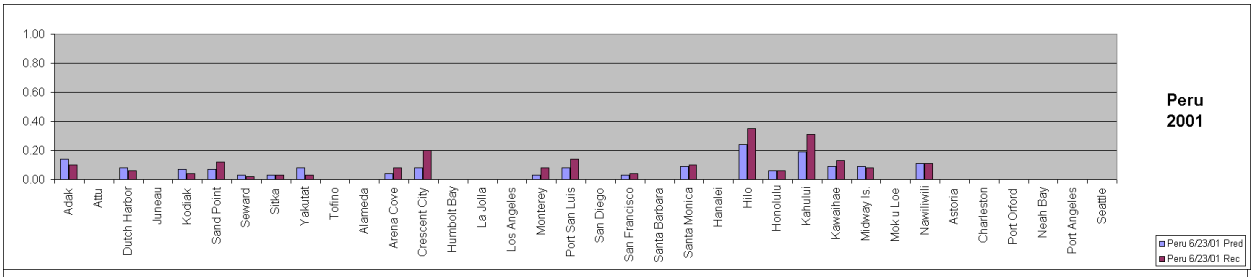
Peru
2001
Peru 6/23/01 Pred
Peru 6/23/01 Rec

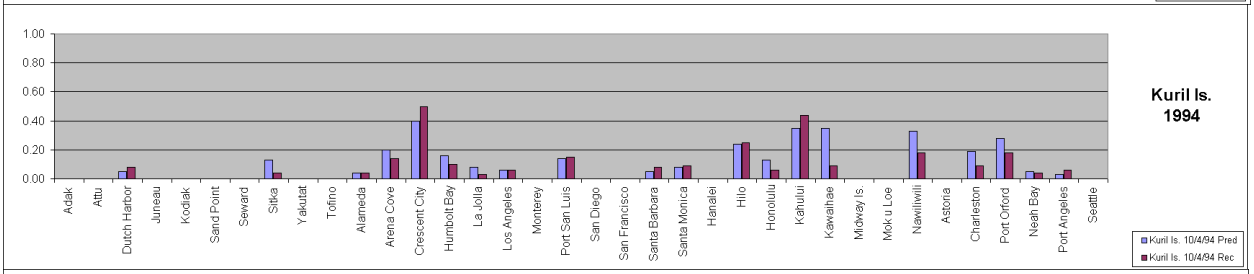
Kuril Is.
1994
Kuril Is. 10/4/94 Pred
Kuril Is. 10/4/94 Rec

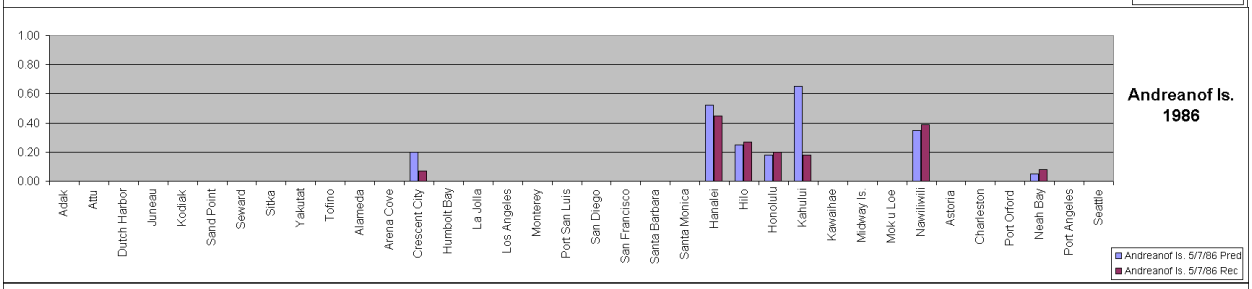
Andreanof Is.
1986
Andreanof Is. 5/7/86 Pred
Andreanof Is. 5/7/86 Rec

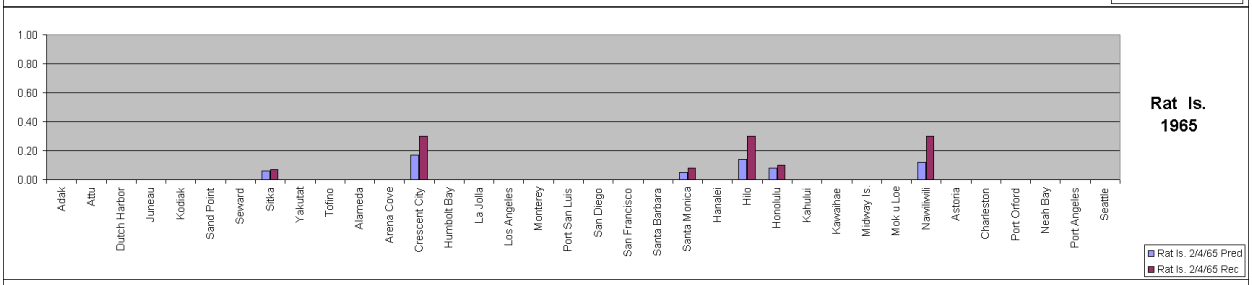
Rat Is.
1965
Rat Is. 2/4/65 Pred
Rat Is. 2/4/65 Rec

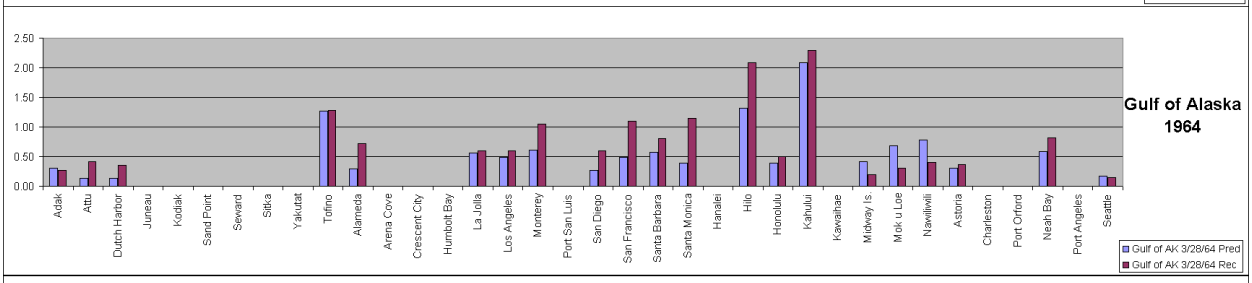
Gulf of Alaska
1964
Gulf of AK 3/28/64 Pred
Gulf of AK 3/28/64 Rec

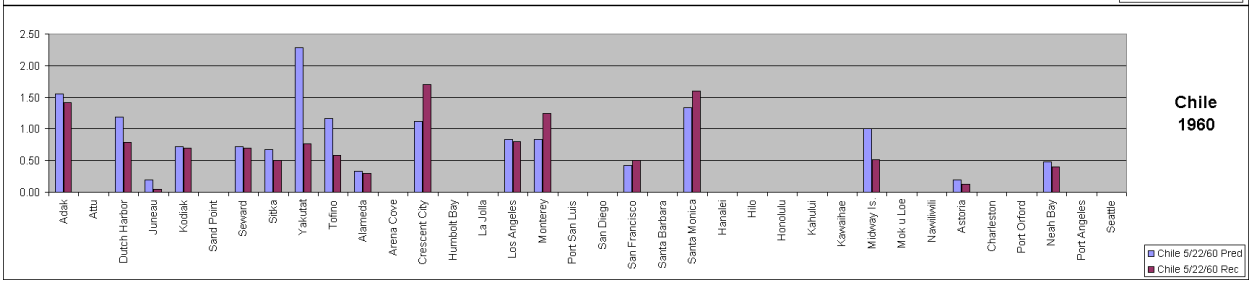
Chile
1960
Chile 5/22/60 Pred
Chile 5/22/60 Rec

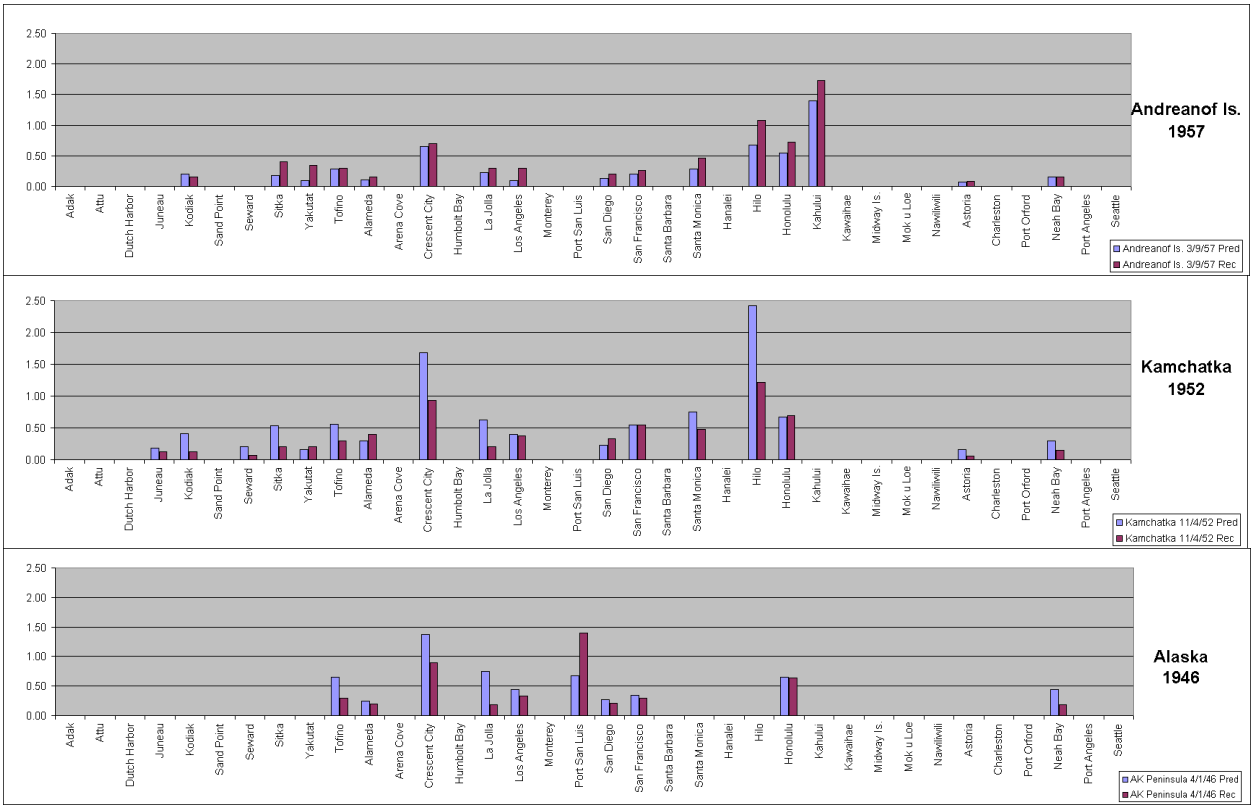

Figure 2. Predicted and recorded tsunami amplitudes (in meters) for the nine events. Notes on each model:

2001 Comparison model is Mw=8.2 located off the northern Chile coast. DART buoy 125 had not been installed at the time of this tsunami so is not available for scaling. The nearest modeled sites were used instead: San Diego – 0.05m, Los Angeles – 0.05m, La Jolla – 0.05m.

1994 Comparison model is Mw=8.2 located off the east coast of Hokkaido, Japan. Scaling sites are: Shemya – 0.15m, Adak – 0.15m, Midway Is. – 0.27m.

1986 Comparison model is Mw=8.2 located south of the Andreanof Is, Alaska. Scaling sites are: Adak – 0.90m, Midway Is. – 0.32m, Dutch Harbor – 0.15m, Sand Point – 0.10m.

1965 Comparison model is Mw=9.0 located south of the Rat Is., Alaska. Scaling sites are: Attu – 1.37m, Midway Is. – 0.20m, Dutch Harbor – 0.20m.

1964 Comparison model is Mw=9.0 located in the eastern Gulf of Alaska. The chosen model was not the most representative of the actual fault break. The model was chosen as it was the closest to the epicenter (which was located at the eastern edge of the fault zone). Scaling sites are: Sitka – 2.1m, Yakutat – 1.5m, Juneau – 1.0m.

1960 Comparison model is Mw=9.5 located off the southern Chile coast. No Hawaiian sites are predicted here as the tide gage observations could not be compared. Predicted heights for some Hawaiian sites are Hilo – 5.58m, Kahului – 4.33m, and Nawiliwili – 1.54m. Scaling sites are: La Jolla – 0.5m, San Diego – 0.7m, Honolulu – 1.07m, Mok u Loe – 0.22m.

1957 Comparison model is Mw=8.2 located south of the Andreanof Is., Alaska. Scaling sites are: Dutch Harbor – 0.70m, Midway Is. – 0.53m, Attu – 0.60m.

1952 Comparison model is Mw=9.0 located off the east coast of Kamchatka. The chosen model was not the most representative of the actual fault break. This model was chosen as it was the closest to the epicenter (which was located at the northern edge of the fault zone). This model is north of the fault rupture. Scaling sites are: Adak – 1.1m, Dutch Harbor – 0.6m, Midway Is. – 1.3m.

1946 Comparison model is Mw=8.2 located near the Shumagin Is., Alaska. Only one Hawaiian site is compared as other tide gage observations could not be obtained. Predicted heights for other Hawaiian sites are Hilo – 1.54m, Kahului – 3.35m, Nawiliwili – 1.30m. Scaling sites: Adak – 0.2m, Yakutat – 0.33m, Sitka – 0.48m.

Site	Amp. (m)	Damage	Year
Los Angeles, CA	0.33	None	1946
Yakutat, AK	0.33	None	1946
Attu, AK	0.3	None	1944
Shemya, AK	0.35	None	1996
Los Angeles, CA	0.38	None	1952
Yakutat, AK	0.4	None	1987
Sitka, AK	0.4	None	1957
Alameda, CA	0.4	None	1952
Santa Monica, CA	0.48	None	1952
Sitka, AK	0.48	None	1946
Sitka, AK	0.5	None	1960
La Jolla, CA	0.5	None	1960
San Francisco, CA	0.5	Strong currents stops ferry	1960
Port Hueneme, CA	0.5	None	1957
Crescent City, CA	0.5	Mooring broke loose	1963
Shelter I., CA	0.5	Boat/dock damage	1957
Adak, AK	0.51	None	1996
San Francisco, CA	0.54	None	1952
Los Angeles, CA	0.6	$200K damage to boats	1964
Monterey, CA	0.6	2 almost drown	1957
San Diego, CA	0.6	Strong current, boat damage	1964
Newport, OR	0.6	None	1960
Tokeland, WA	0.6	None	1960
Brandon, OR	0.6	None	1946
Kodiak, AK	0.6	None	1946
Attu, AK	0.6	None	1957
Ketchikan, AK	0.6	None	1964
Dutch Harbor, AK	0.6	None	1952
Crescent City, CA	0.7	None	1957
San Diego, CA	0.7	Boat/pier damage (20 Knot current)	1960
Port Hueneme, CA	0.7	None	1952
Dutch Harbor, AK	0.7	None	1957
Yakutat, AK	0.76	None	1960
Dutch Harbor, AK	0.79	None	1960
Unga, AK	0.8	Dock swept away	1946
Port Hueneme, CA	0.8	RR tracks flooded	1946
San Pedro, CA	0.8	Wharf flooded	1868
Avila, CA	0.8	None	1927
Santa Barbara, CA	0.8	Boat damage	1964
Los Angeles, CA	0.8	$1M damage, 1 drowning	1960
Adak, AK	0.9	None	1986
Shemya, AK	0.9	None	1969
DePoe Bay, OR	0.9	None	1946
Crescent City, CA	0.9	None	1946
Santa Barbara, CA	0.9	None	1946
Yakutat, AK	0.9	Mooring broke	1958
Santa Cruz, CA	0.9	Boats loose, swift currents	1960
Trinidad, CA	0.9	Cars stuck on beach	1992
Pacific Grove, CA	0.9	None	1960
Avila, CA	0.9	None	1960

Table 2. Tsunami damage listed with tsunami amplitude. Impact information from Lander, *et al*. (1993) and Lander (1996).

TSUNAMI DAMAGE VERSUS AMPLITUDE

When regional tsunami warnings are initially issued, the expected tsunami amplitude is unknown. Using the technique described in this report, tsunami amplitudes can be predicted outside the source zone. For tsunami warning purposes, an amplitude threshold must be chosen such that if predicted amplitudes are above this threshold outside the source zone, the warning will be expanded. Conversely, if predicted amplitudes outside the source zone are lower than the threshold, the warning will be cancelled or restricted to the source area.

To determine the proper amplitude threshold, historic tsunamis in the WC/ATWC AOR are examined. Table 2, based on the works of Lander, *et al.*, (1993) and Lander (1996), lists damage along with corresponding tsunami amplitude. Several other recorded tsunamis greater than 1m amplitude have occurred in the WC/ATWC AOR and are clearly dangerous. These are not listed in the table. Based on the damage/amplitude comparison shown in Table 2, tsunamis above 50cm must be considered potentially dangerous. If tsunami amplitudes are expected to be above 50cm outside the source zone, the warning should be expanded.

DISCUSSION

Based on a 50cm amplitude warning threshold level, Table 3 lists warning expansion decisions for the nine tested events. The maximum predicted amplitude outside the source region within the AOR and its location are also given. All damaging tsunamis tested would have prompted an expanded warning (1946, 1952, 1957, 1960, and 1964). All non-damaging tsunamis outside the source zone would not have prompted an expanded warning (1965, 1986, 1994, and 2001). During the actual events, both the 1986 and 1994 events triggered warnings which covered the entire WC/ATWC AOR. These warnings were considered "false" by most emergency managers. If the numerical backing provided by this predictive amplitude technique had existed at the time of those two warnings, it is likely that warnings would have been restricted to AOR regions nearest the epicenters.

Source Region	Date	Maximum predicted amp. outside source zone within AOR (m)	Warning expansion decision
Peru	2001/6/23	0.14 – Adak, AK	No
Kuril Is.	1994/10/4	0.40 – Crescent City, CA	No
Aleutian Is.	1986/5/7	0.21 – Rio Del Mar, CA	No
Rat Is.	1965/2/4	0.18 – Port Orford, OR	No
Gulf of Alaska	1964/3/28	1.93 – Arena Cove, CA	Yes
Southern Chile	1960/5/22	2.49 – Attu, AK	Yes
Aleutian Is.	1957/3/9	0.65 – Crescent City, CA	Yes
Kamchatka	1952/11/4	1.68 – Crescent City, CA	Yes
Alaska Peninsula	1946/4/1	1.44 – Half Moon Bay, CA	Yes

Table 3. Warning expansion decision summary for the nine tested events. "Outside the source zone" indicates areas not included in the initial warning region.

A few potential problems with the method should be noted. Tide gages in the immediate vicinity of the source may record localized effects, such as waves generated by sub-sea landslides. The models are based strictly on earthquake-related sea floor displacement. Scaling the model with tide gage data which includes a secondary component will lead to over-estimating the amplitude outside the source zone. To help prevent this effect, where feasible only tide gage or DART data from outside the immediate source zone should be used.

Another potential problem occurs for great earthquakes with large fault length and a unidirectional rupture. In this case the wrong model may be chosen based on the epicenter location. For example, the 1952 and 1964 earthquakes had rupture lengths over 500km and were mainly unidirectional rupture (Kanamori, 1976; Kanamori, 1970). For both cases, a different magnitude 9.0 model was chosen in this test than would have been selected had the areal extent of the fault zone been known. Predicted amplitudes for both events were still adequate for warning purposes, though, due to the scaling process.

Amplitude prediction using this technique could lead to a two level tsunami warning scheme. Historic tsunami impacts have shown that amplitudes between 0.5 and 1.0m have not induced major inundation damage (Table 2). Tsunami damage in this range is limited to boat and dock damage along with danger to swimmers. When a tsunami in this range is expected, a Level 1 or "clear-the-beach" warning would be more appropriate than a complete evacuation to some pre-determined maximum inundation line. If amplitude predictions were greater than 1m, or no prediction could be made, a Level 2 or full warning would be issued. Due to assumptions made in the tsunami models, predicted amplitudes greater than 1m may indicate a much greater inundation level. Splitting warnings into 2 levels would reduce unnecessary evacuations and yet still provide needed protection to those near the waterfront.

The predictive technique tested in this report can be improved with the addition of near real-time fault dimension determinations, real-time tsunami propagation models, improved scaling procedures, and inclusion of inundation. With the present limitations, though, it is shown here to be sufficiently accurate to use as a tool to aide in tsunami warning expansion, cancellation, and restriction decisions.

DISCLAIMER

The views expressed are those of the author and do not necessarily represent those of the National Weather Service.

ACKNOWLEDGEMENTS

Thanks to Rich Przywarty and James Partain of the National Weather Service/Alaska Region for continued support of the tsunami modeling effort, Zygmunt Kowalik of the University of Alaska, Fairbanks for transferring his numerical techniques to the WC/ATWC, Bruce Turner of the WC/ATWC for ideas on this project, and Tom Sokolowski, formerly of the WC/ATWC, for spear-heading the tsunami modeling effort in 1988.

REFERENCES

Bernard, E.N., F.I. Gonzalez, C. Meinig, and H.B. Milburn (2001). Early detection and real-time reporting of deep-ocean tsunamis, Proceedings of the International Tsunami Symposium 2001 (ITS 2001) (on CD-ROM), 97-108.

Kanamori, H. (1976). Re-examination of the earth's free oscillations excited by the Kamchatka earthquake of November 4, 1952, *Physics of the Earth and Planetary Interiors*, **11**, 216-226.

Kanamori, H. (1970). The Alaska earthquake of 1964: radiation of long-period surface waves and source mechanism, *Journal of Geophysical Research*, **75**, 5029-5040.

Kowalik, Z and P. M. Whitmore (1991). An investigation of two tsunamis recorded at Adak, Alaska, *Science of Tsunami Hazards*, **9**, 67-83.

Lander, J. F. (1996). Tsunamis affecting Alaska 1737-1996, NGDC Key to Geophysical Research Documentation No. 31, USDOC/NOAA/DESDIS/NGDC, Boulder, CO, USA, 195 pp.

Lander, J. F., P. A. Lockridge, and M. J. Kozuch (1993). Tsunamis affecting the west coast of the United States 1806-1992, NGDC Key to Geophysical Research Documentation No. 29, USDOC/NOAA/DESDIS/NGDC, Boulder, CO, USA, 242 pp.

Okada, Y. (1985). Surface deformation due to shear and tensile faults in a half-space, *Bulletin of the Seismological Society of America*, **75**, 1135-1154.

Whitmore, P. M. and Sokolowski, T. J. (1996). Predicting tsunami amplitudes along the North American coast from tsunamis generated in the northwest Pacific Ocean during tsunami warnings, *Science of Tsunami Hazards*, **14**, 147-166.